Fig. 1.

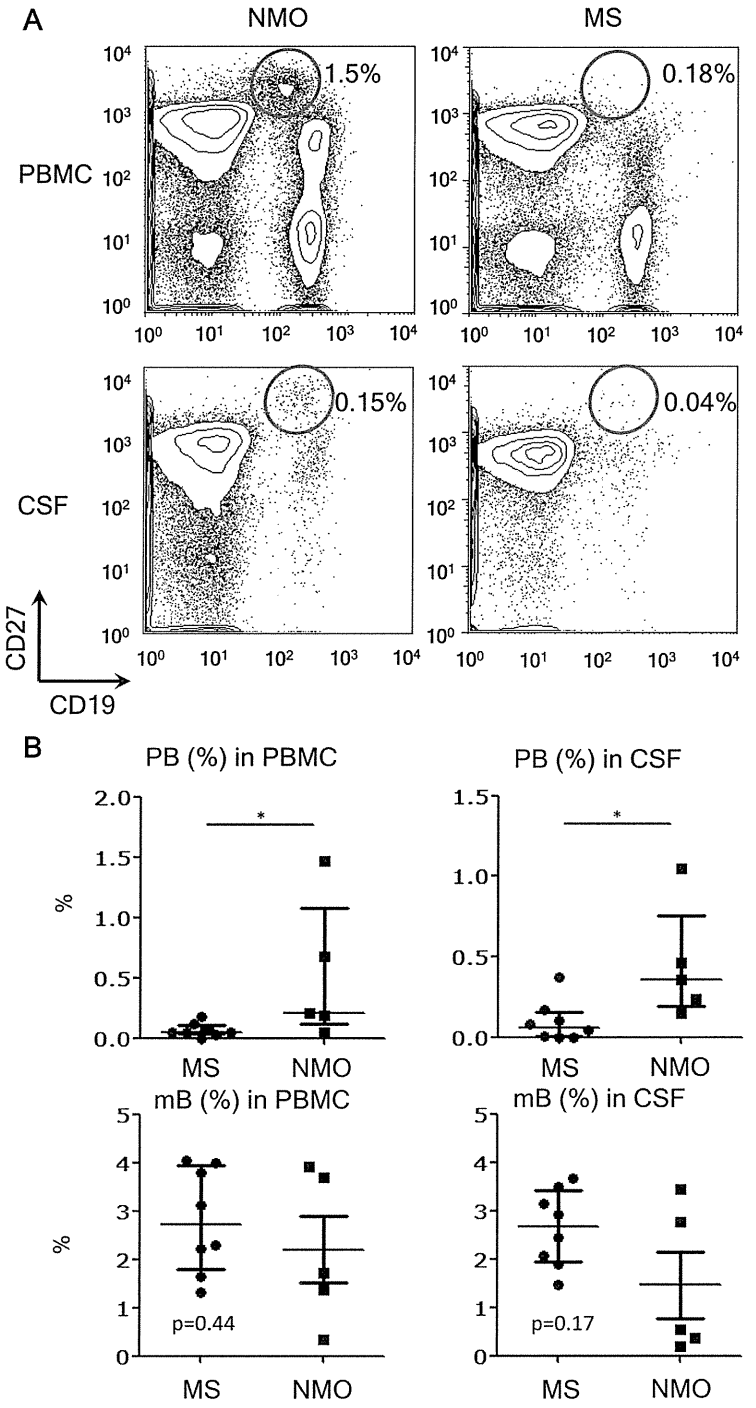

Figure 1. Selective increase of plasmablasts (PBs) during relapse of NMO. (A) B-cell subpopulation analysis by flow cytometry. Peripheral blood mononuclear cell (PBMC) and cerebrospinal fluid (CSF) cells were obtained during relapse of neuromyelitis optica (NMO) or multiple sclerosis (MS) and were stained with fluorescence-conjugated anti-CD19, -CD27, -CD38, and -CD180 monoclonal antibodies (mAbs). PB cells ($CD19^{int}CD27^{high}$) were encircled after observing that they also bear the phenotype of $CD38^{high}CD180^{-}$ (Figure S1). Values represent the percentages of PB cells among all mononuclear cells.
(B) The proportion of PB and memory B-cells (mB) in PBMC and CSF from MS and NMO during relapse. The data were obtained from eight patients with MS and five with NMO [*$p < 0.05$ by Mann–Whitney test; each error bar represents the median ± interquartile range (IQR)].

doi: 10.1371/journal.pone.0083036.g001

cell marker CD138 [12]. CD138 is known to be an adhesion molecule as well as a negative regulator of cell migration [23]. Both $CD138^+$ and $CD138^-$ PBs are able to produce AQP4-Ab [12]. However, the mutual relationship of these PB subsets remained obscure. The expression of HLA-DR was examined, because PB cells that produce IgG autoantibodies reportedly express HLA-DR [24]. We found that only the proportion of $CD138^+HLA\text{-}DR^+$ PBs significantly increased during the relapse of NMO, compared with remission (Figure **2A**). More importantly, we found that the $CD138^+HLA\text{-}DR^+$ PBs comprised the vast majority of PBs in the CSF of NMO patients in relapse (Figure **2B**). Since CD138 is thought to be upregulated in activated cells [23], we speculated that antibody-producing PB cells ($CD138^+HLA\text{-}DR^+$ PB) were activated in the periphery in the patients during relapse, and that they might preferentially be recruited to the CSF and be further activated.

$CD138^+HLA\text{-}DR^+$ PB cells represent recently differentiated IgG-producing PBs

Previous studies showed that activated PB cells secreting IgGs would increase in the peripheral blood of healthy individuals after receiving vaccination [25,26]. To strengthen our postulate that $CD138^+HLA\text{-}DR^+$ PBs are recently activated IgG-secreting PBs, we also characterized the PB phenotypes in healthy vaccinated individuals. We found that proportions of $CD138^+$ PBs, but not $CD138^-$ PBs, among $CD19^+$ B-cells significantly increased one week after influenza vaccination. Neither mB nor naïve B-cells (nB) were altered (Figure **3A**). This observation suggests that $CD138^+$ PB cells are more enriched among germinal center-derived cells than $CD138^-$ PB. Next, we compared $HLA\text{-}DR^+$ and $HLA\text{-}DR^-$ PBs from vaccinated individuals for the intracellular expression of IgGs. We confirmed that $HLA\text{-}DR^+$ PBs were the major producer of IgGs (Figure **3B**). These results support further that $CD138^+HLA\text{-}DR^+$ PBs, which increase during the relapse of NMO, correspond to recently activated IgG-producing cells.

$CD138^+HLA\text{-}DR^+$ PBs upregulate CXCR3 during relapse of NMO

Results of chemo-attractant assays showed that CXCR4 and CXCR3 ligands would attract PB cells, but not mature plasma cells [27]. The expression of CXCR4 on PB is important for their homing to the bone marrow, whereas the interaction of CXCR3 with its ligand CXCL10 plays a key role in the migration of PBs toward inflamed tissues. CXCL10 is thought to play a critical role in NMO [17]. Therefore, we analyzed the expression of CXCR4 and CXCR3 on PB cells in the peripheral blood of NMO patients. We observed that the expression levels of CXCR3 on PBs or activated PBs ($CD138^+HLA\text{-}DR^+$) were significantly higher during relapse than in remission of NMO. It appeared that the upregulation of CXCR4 on PBs during relapse was less obvious (Figure **4A**). We further analyzed the PBMC obtained during relapse and in remission for the expression of CXCR3 and CXCR4 according to B-cell subpopulations. Proportions (%) of $CXCR3^+$ cells among mB and nB cells were 17% and 2%, respectively during relapse and did not differ from remission, whereas that for PBs was approximately 50% during relapse compared to 23% in remission (Figure **4B**). In contrast, the percentages of $CXCR4^+$ cells were higher in mB and nB cells (50% and 56%, respectively) than that in PBs (15%) during relapse. These percentages of $CXCR4^+$ B-cell subpopulations did not differ from those during remission. The increased CXCR3 expression on PBs during relapse suggests biological significance and allows us to speculate that the migration of $CD138^+HLA\text{-}DR^+$ PBs to the CNS might involve a CXCR3-dependent mechanism.

Peripheral PBs and CSF PB have common IgG variable regions

Single-cell sorting of lymphocytes is a refined method for characterizing the cellular properties of human B-cell lineages [10,21,25,28]. To characterize the antibody gene repertoire of the IgG-producing PBs in patients with NMO, we performed a single-cell sorting of PB clones from peripheral blood and CSF during relapse of NMO, and sequenced the gene fragments of the heavy and light chain variable regions after cloning. In principle, B-cell V regions are rearranged within the germinal centers and acquire the ability to produce high-affinity antibodies that are diversified by somatic hypermutation. We compared these variable region sequences with the germline database of IgBLAST (www.ncbi.nlm.nih.gov/igblast/) to estimate the number of mutations. In addition, the ratio of replacement to silent mutations (R/S ratio) was analyzed in single-cell sorted PBs derived from a patient with NMO. We established 38 paired vector clones containing cDNAs of heavy- and light-chain variable regions. The variable regions of the PB IgG heavy chain contained an average of 17 mutations and had higher R/S ratios in CDRs than in framework regions (FR) (Figures **S4** and **S5**). Moreover, the variable regions of the IgG κ chains of the sorted PB contained an average of 10 mutations and also had higher R/S ratios in CDRs than in FR. However, there were no significant differences in the number of mutations between the PB clones from peripheral blood and from CSF (Figure **S6**). The numbers of mutations in these PB clones did not differ from those in IgG^+ mB [28]. These results confirmed that PB clones derived from NMO would represent a post-germinal center B-cell lineage.

The similarity in the numbers of mutations in peripheral and CSF PB clones prompted us to address whether differentiated PBs might migrate from peripheral blood to CSF without further affinity maturation. Therefore, we compared the sequences of the CDR regions of PB clones from peripheral blood and CSF. Single-cell sorted PBs (109 from peripheral blood and 67 from CSF) were obtained from two patients with NMO in relapse. Because our target was recently differentiated PB derived from germinal centers, we selectively amplified the CDR3 regions of the IgG H-chains. The CDR3 regions of the IgG genes (41 from patient 1 and 51 from patient 2) were successfully sequenced. The clones were numbered in the order they were collected. We noticed that 11 CDR3 sequences were repeatedly detected in 17 CSF PB clones and 21 peripheral blood PB clones (Table **2**). Interestingly, five of the 11 sequences were detected in both peripheral blood and CSF clones of the same patient (clone numbers in bold), indicating the migration of the PB clones from the peripheral blood to the CSF. Interestingly, a common

Fig. 2.

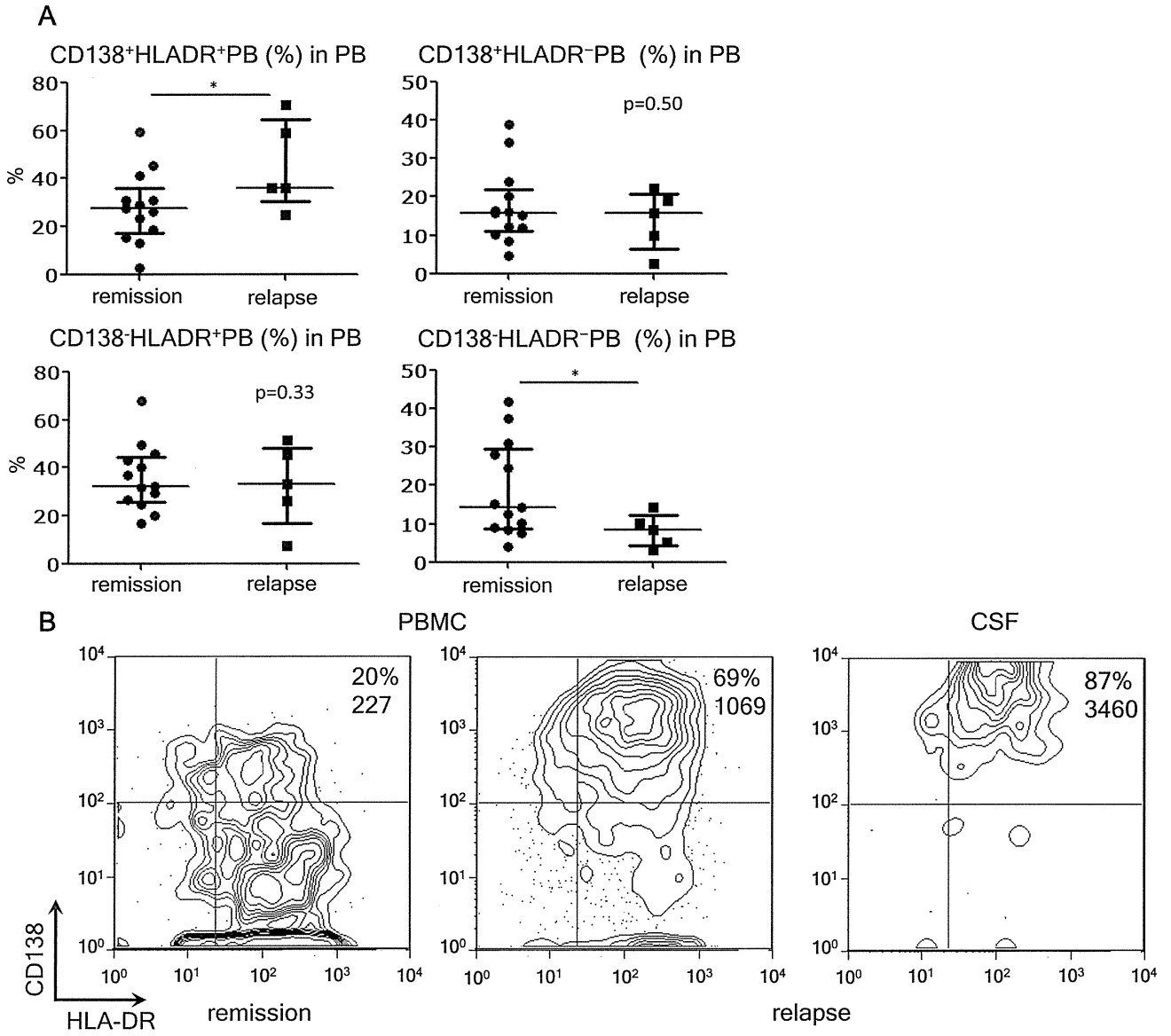

Figure 2. Kinetics of CD138$^+$HLA-DR$^+$ PB during relapse of NMO. (A) Analysis of pooled peripheral blood mononuclear cells (PBMC) data from neuromyelitis optica (NMO) in remission and relapse. The plasmablasts (PBs) were subdivided into four subpopulations by considering the expression of CD138 and HLA-DR. The individual data show the percentages of each PB subpopulation among the total PB [*$p < 0.05$ by Mann–Whitney test; each error bar represents the median ± interquartile range (IQR)].

(B) Enrichment of CD138$^+$HLA-DR$^+$ PBs in the CSF. The PBMC and CSF cells were obtained from NMO during relapse. The values indicate the percentages of CD138$^+$HLA-DR$^+$ PBs among the total PB. The expression level of CD138 was assessed by mean fluorescence intensity (MFI). Representative data of one out of three different cases are shown.

doi: 10.1371/journal.pone.0083036.g002

CDR3 sequence (VKFSATAAAGNWDHFDY) was obtained from the PB clones from both patients (peripheral blood-derived clones 28 and 30 and CSF-derived clone 36 in patient 1; peripheral clones 3 and 24 and CSF-derived clones 1, 2, and 22 in patient 2 with the CDR3 sequence). These results suggested that the PBs seem to be inclined toward several representative clones during the relapse of NMO. Although the pathological implications remain obscure, it might be important to follow up in a larger patient cohort.

Fig. 3.

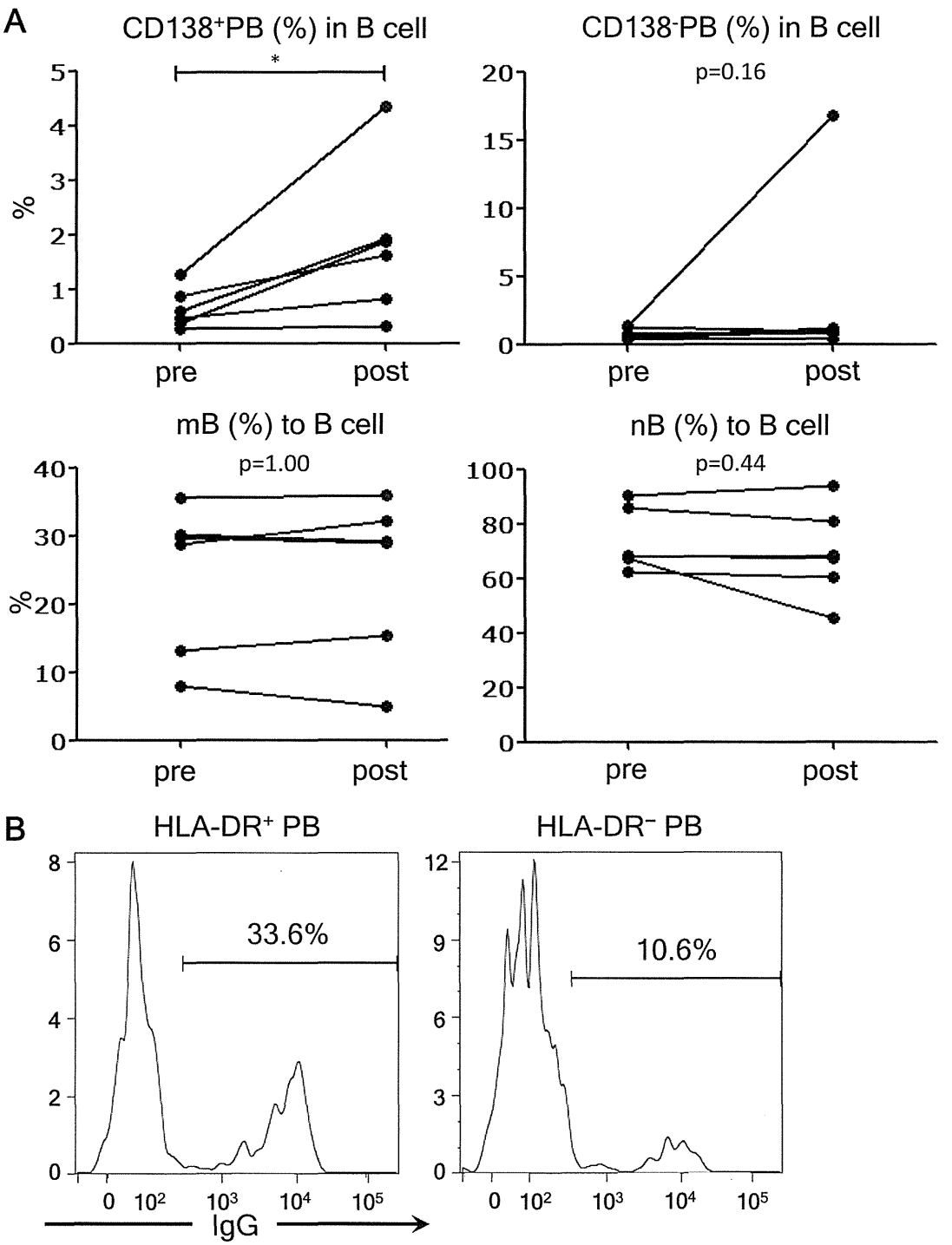

Figure 3. CD138⁺HLA-DR⁺ plasmablasts (PB) cells are recently differentiated IgG-producing PB. (A) The effects of influenza vaccination on the frequencies of B-cell subpopulations were analyzed. The frequency of each B-cell subpopulation derived from the peripheral blood of healthy subjects before (pre) and seven days after vaccination (post) is shown. Each line connects the values obtained from a single subject (*$p < 0.05$ by Wilcoxon signed rank test).
(B) The results of intracellular IgG staining of HLA-DR⁺ PB (left) and HLA-DR⁻ PBs (right) are shown. The values represent the percentages of IgG-producing cells in each PB subpopulation. Representative data of one out of three individuals are displayed.
doi: 10.1371/journal.pone.0083036.g003

Fig. 4.

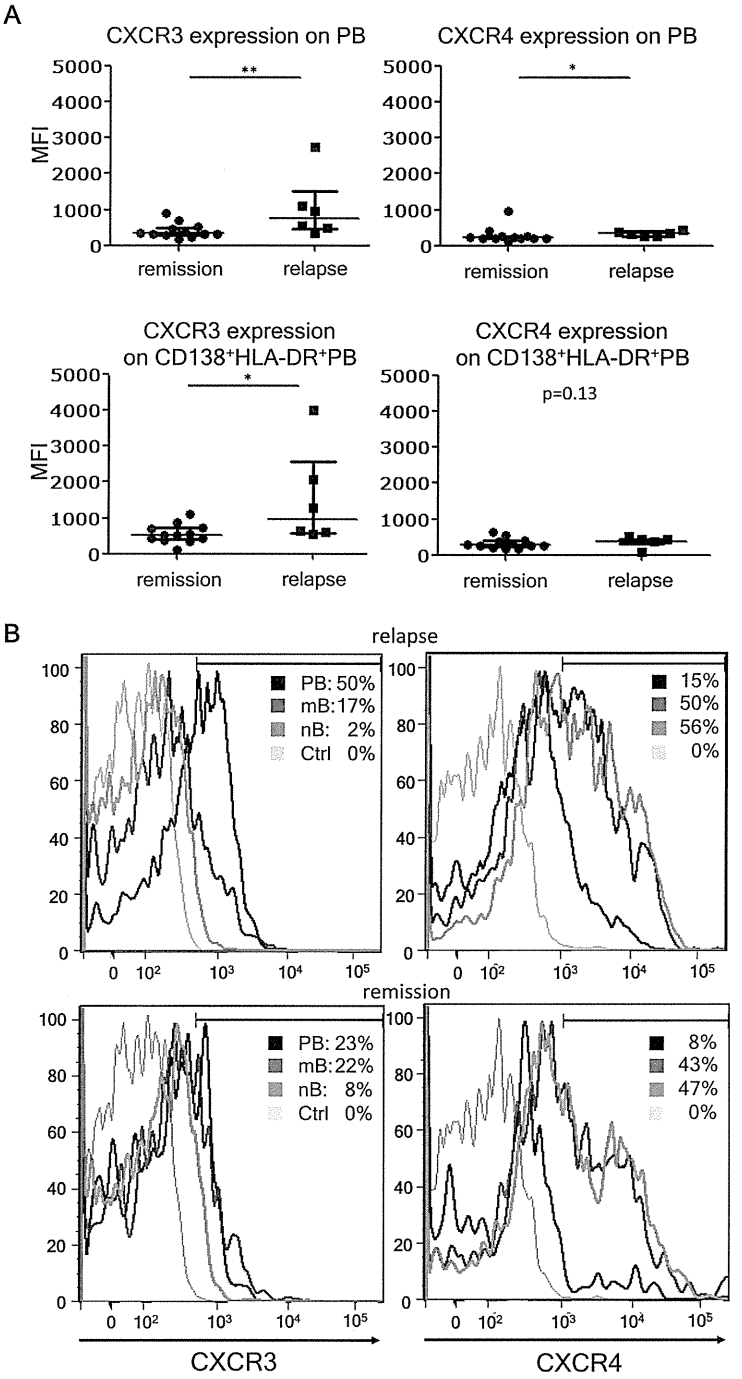

Figure 4. CXCR3 expression on plasmablasts (PBs) correlates with the disease state. (A) CXCR3 and CXCR4 on PB in neuromyelitis optica (NMO) relapse and remission. Here, we compared the mean fluorescence intensity (MFI) of CXCR3 and CXCR4 expression in the peripheral blood PBs during remission and relapse of NMO. MFI of CXCR3 and CXCR4 expressions on $CD138^+HLA\text{-}DR^+$ PBs were also analyzed [**p < 0.01 and *p < 0.05 by Mann–Whitney test; each error bar represents the median ± interquartile range (IQR]].

(B) B-cell subpopulations derived from peripheral blood mononuclear cells (PBMC) during disease relapse and remission were analyzed by flow cytometry to investigate the expression of CXCR3 and CXCR4. The values represent the percentages of $CXCR3^+$ or $CXCR4^+$ cells within each B-cell subpopulation. Unstained control of PBMC is indicated by Ctrl. Representative data of at least five patients in each disease state are shown.

doi: 10.1371/journal.pone.0083036.g004

Table 2. V_H sequences of the plasmablasts (PBs) clones.

Clones derived from peripheral blood	Clones derived from the cerebrospinal fluid (CSF)	H chain of CDR3	Germline	Joint region
pt1-**28, 30**	**36**	VKFSATAAAGNWDHFDY	VH3-23	J4
pt1-**26**	**12, 15**	ARGFYYGSGSRRGMDV	VH4-4	J6
pt1-22, 23	—	ARGDNGSFSY	VH3-74	J4
pt1-□	8, 13	ARGIVTA	VH3-7	J4
pt1-□	34, 39	ARQATEQVPVLPFVMGAPRKKGGAFNV	VH4-39	J4
pt2-33, 37, 39	—	VRDSPPPATHFDY	VH3-21	J4
pt2-**27**	**25, 30, 32, 35, 36, 40**	ARMARAGNYANNWYDP	VH4-59	J4
pt2-**3, 24**	**1, 2, 22**	VKFSATAAAGNWDHFDY	VH3-23	J4
pt2-**4, 6, 10, 12, 13, 20**	**8**	AREDLPGTMFDY	VH3-33	J4
pt2-23, 26	—	VRDNWGVDY	VH3-74	J4
pt2-21, 31	—	RCHRDRSGSPVGWYAP	VH4-30	J4

The IgG heavy chain sequences in the PB clones from neuromyelitis optica (NMO) patients were determined. Distinct PB clones obtained from peripheral blood and CSF samples are numbered in the order they were collected. In the table are shown the amino acid sequences of 11 CDR3 that were repeatedly detected in the PB clones, V_H gene (germline), and joint regions. When the same sequences were detected in both peripheral blood and CSF clones of the same patient, the clone numbers were highlighted in bold.

doi: 10.1371/journal.pone.0083036.t002

Discussion

NMO is an inflammatory disease with a pathology characterized by AQP4-Ab–mediated astrocytopathy in the CNS lesions. As previously reported, IL-6 as well as IL-6-dependent PBs, a terminally differentiated B-cell population, are involved in the pathogenesis [12]. Results of laboratory works have suggested that the AQP4-Ab produced in the periphery might cause the astrocyte pathology [9–11], assuming that they could enter the CNS through the disrupted area of the BBB. However, the role of antibody production within the CNS has not been excluded in human NMO. In fact, it remains unclear why AQP4-expressing organs, including kidney and stomach, are not involved in NMO, despite the presence of AQP4-Abs in the periphery [29]. It is unknown whether PBs play a pathogenic role within the CNS after migrating to the CNS. Here, we demonstrated that CSF lymphocytes from NMO during relapse are enriched in activated PB cells, brightly expressing CD138 and HLA-DR. CD138 serves not only as a negative regulator of cell migration in vitro [23], but also as the marker of tissue migrating plasmablasts/plasma cells in vivo [27]. We have confirmed that HLA-DR expression would characterize the PB subset capable of secreting IgG in healthy vaccinated subjects (Figure **3B**). It is possible that the increased frequency of HLA-DR$^+$ PBs in NMO reflects an antigen-driven B-cell activation that plays a key role in NMO pathogenicity. Moreover, we showed that the CD138$^+$HLA-DR$^+$ PBs would selectively upregulate CXCR3 during relapse. Because CXCL10, a CXCR3 ligand, is present in the CSF of NMO [17], we speculate that the activated PBs might migrate from the periphery to the CNS in a CXCR3-dependent manner. Intriguingly, a study on a neurotropic coronavirus-induced encephalomyelitis model showed that CXCR3-expressing PBs would infiltrate the CNS and locally produce antibodies against the pathogen [30]. The viral encephalomyelitis induced in CXCR3-knockout mice was remarkably exacerbated in association with a marked reduction of PB cells infiltration. Although this work highlights the importance of CXCR3-dependent PB migration in the production of antiviral antibodies within the CNS, it also gives us a clue to understand how migratory PBs would contribute to the pathogenesis of NMO.

We further proved that IgG-producing PBs in the CSF during relapse share identical CDR sequences with those from PBs in the peripheral blood (Table **2**). The IgG sequences were highly mutated (Figure **S4** and **S5**), indicating that helper T-cells guided the PBs toward germinal centers. Although we did not separate CD138$^-$ and CD138$^+$ PBs in this analysis, the number of mutations in the H-chain variable regions showed a single-peak distribution (Figure **S4**). These results suggest that both CD138$^-$ and CD138$^+$ PBs are affinity-maturated B-cells, although CD138 expression levels could inversely correlate with the tissue-migrating ability [23]. There remained a possibility that mB might give rise to PBs within the CSF. However, further affinity maturation in PBs was not observed in CSF compared with peripheral blood, indicating that clonal expansion and differentiation of mB in the CSF is not a major pathway. This assumption is also supported by the rare occurrence of CSF oligoclonal bands and raised IgG index in NMO, which indicates that the intrathecal IgG synthesis was low, transient, and restricted to acute relapse in NMO patients [6,31]. Taken together, it is likely that CXCR3-expressing PBs are expanded in the periphery and recruited to the CNS in the pathogenesis of NMO. In the CNS, B-cell stimulatory cytokines such as IL-6 would support the PB survival and AQP4-Ab production, leading to the destruction of astrocytes and the glia limitans. We and another group have shown that PBs from peripheral blood and CSF produce anti-AQP4 IgG antibody in NMO [10,12]. We therefore postulated that the common IgGs shared by PBs from the PBMC and CSF (Table 2) could bind to AQP4. Despite substantial efforts, however, we have not succeeded in this attempt so far. Though we speculate that peripherally expanded PBs producing anti-AQP4 should be able to cross BBB like other PBs, irrespective of the antigen

specificity, more efforts will be needed to formally prove our postulate.

We previously demonstrated the role of IL-6-dependent PBs in the production of AQP4-Ab [12]. In the present report, we indicate that PBs may play a more critical role in the CNS by locally producing AQP4-Ab. The relevance of this model can be verified in clinical trials of drugs targeting appropriate cells or molecules. In fact, we have recently shown that humanized anti–IL-6 receptor antibody (Tocilizumab) was efficacious in a patient with NMO in reducing the number of PBs in the peripheral blood as well as stabilizing the clinical conditions [32]. In another report, Tocilizumab successfully controlled three NMO patients who were resistant to the anti-CD20 antibody Rituximab [33]. These results indicate that PBs, rather than $CD20^+$ mB, play a pivotal role in NMO. Therefore, it will be intriguing to test the effect of drugs altering the migration of PBs toward the CNS [34].

Supporting Information

Figure S1. Flow cytometric analysis of PB. Flow cytometric scheme of B-cell subpopulation analysis. The partitioned cells are $CD19^+CD27^+$ cells within peripheral blood mononuclear cells (PBMC; left panel). The $CD19^+CD27^+$ cells were further analyzed to investigate the expression of CD38 and CD180 (middle panel). $CD38^{high}CD180^-$ cells (partitioned in the middle panel), corresponding to plasmablast (PB) cells, were analyzed again to investigate the expression of CD19 and CD27 (right panel). This result assured that the encircled population in Figure 1A represented $CD19^{int}CD27^{high}CD38^{high}CD180^-$ PB cells.
(TIF)

Figure S2. B-cell proportions in peripheral blood mononuclear cells (PBMC) and cerebrospinal fluid (CSF) from NMO and MS. PBMC and CSF were obtained from neuromyelitis optica (NMO) and multiple sclerosis (MS) patients. Here, we show the proportions (%) of total B-cells ($CD19^+$) and $CD19^+CD27^+$ cells among the PBMC and CSF. The Mann-Whitney test provided the statistical p values. The bars represent the median ± interquartile range (IQR).
(TIF)

Figure S3. The proportion of plasmablast (PB) cells among the total B-cells. Peripheral blood mononuclear cells (PBMC) and cerebrospinal fluid (CSF) were obtained from neuromyelitis optica (NMO) and multiple sclerosis (MS) patients. The proportions (%) of PB cells among the total B cells ($CD19^+$) are reported. The Mann-Whitney test provided the statistical p values (**$p < 0.01$; *$p < 0.05$). The bars represent the median ± interquartile range (IQR).
(TIF)

Figure S4. The number of somatic hypermutations in plasmablast (PB) clones. V_H and V_{Kappa} regions of the IgG gene were evaluated in a total of 38 PB clones derived from a patient with neuromyelitis optica NMO (Pt1) during relapse. There were 17.4 ± 1.3 [mean ± standard error of the mean (SEM)] in the V_H regions and 10.5 ± 1.5 mutations in the V kappa regions.
(TIF)

Figure S5. Plasmablast (PB) cells are diversified by somatic hypermutations. The mutation frequencies in the framework regions (FR) and in complementarity-determining regions (CDR) of the V_H and V_{Kappa} regions of the IgG genes were analyzed in PB clones from patient 1 (Pt1). The ratio of replacement (R, black bars) to silent (S, white bars) changes are shown at the bottom (R/S ratio).
(TIF)

Figure S6. Comparison of the somatic hypermutations in peripheral blood mononuclear cells (PBMC)- and cerebrospinal fluid (CSF)-derived PB clones. Here, we compare the plasmablast (PB) clones derived from the peripheral blood (N = 14) and from CSF (N = 24) with the number of mutations in the V_H and V_{Kappa} regions of the IgG genes. The statistic p values were obtained by Mann-Whitney test. The data represent the median ± interquartile range (IQR).
(TIF)

Acknowledgements

We thank Dr. Toshiyuki Takahashi and Dr. Kazuo Fujihara (Tohoku University) for performing the assays of AQP4-Ab detection.

Author Contributions

Conceived and designed the experiments: NC TA SO SM TY. Performed the experiments: NC TM. Analyzed the data: NC TA TM MN TY. Contributed reagents/materials/analysis tools: HK KY YK NH TO MM TT. Wrote the manuscript: NC TA TY. Supervised the work: TY.

References

1. Wingerchuk DM, Hogancamp WF, O'Brien PC, Weinshenker BG (1999) The clinical course of neuromyelitis optica (Devic's syndrome). Neurology 53: 1107-1114. doi:10.1212/WNL.53.5.1107. PubMed: 10496275.
2. Lennon VA, Wingerchuk DM, Kryzer TJ, Pittock SJ, Lucchinetti CF et al. (2004) A serum autoantibody marker of neuromyelitis optica: distinction from multiple sclerosis. Lancet 364: 2106-2112. doi:10.1016/S0140-6736(04)17551-X. PubMed: 15589308.
3. Wingerchuk DM, Lennon VA, Lucchinetti CF, Pittock SJ, Weinshenker BG (2007) The spectrum of neuromyelitis optica. Lancet Neurol 6: 805-815. doi:10.1016/S1474-4422(07)70216-8. PubMed: 17706564.
4. Warabi Y, Matsumoto Y, Hayashi H (2007) Interferon beta-1b exacerbates multiple sclerosis with severe optic nerve and spinal cord demyelination. J Neurol Sci 252: 57-61. doi:10.1016/j.jns.2006.10.008. PubMed: 17125797.
5. Kleiter I, Hellwig K, Berthele A, Kümpfel T, Linker RA et al. (2012) Neuromyelitis Optica Study Group. Failure of natalizumab to prevent relapses in neuromyelitis optica. Arch Neurol 69: 239-245. doi:10.1001/archneurol.2011.216. PubMed: 22332191.
6. Misu T, Fujihara K, Kakita A, Konno H, Nakamura M et al. (2007) Loss of aquaporin 4 in lesions of neuromyelitis optica: distinction from

multiple sclerosis. Brain 130: 1224-1234. doi:10.1093/brain/awm047. PubMed: 17405762.
7. Roemer SF, Parisi JE, Lennon VA, Benarroch EE, Lassmann H et al. (2007) Pattern-specific loss of aquaporin-4 immunoreactivity distinguishes neuromyelitis optica from multiple sclerosis. Brain 130: 1194-1205. doi:10.1093/brain/awl371. PubMed: 17282996.
8. Takano R, Misu T, Takahashi T, Sato S, Fujihara K et al. (2010) Astrocytic damage is far more severe than demyelination in NMO: a clinical CSF biomarker study. Neurology 75: 208-216. doi:10.1212/WNL.0b013e3181e2414b. PubMed: 20644148.
9. Bradl M, Misu T, Takahashi T, Watanabe M, Mader S et al. (2009) Neuromyelitis optica: pathogenicity of patient immunoglobulin in vivo. Ann Neurol 66: 630-643. doi:10.1002/ana.21837. PubMed: 19937948.
10. Bennett JL, Lam C, Kalluri SR, Saikali P, Bautista K et al. (2009) Intrathecal pathogenic anti-aquaporin-4 antibodies in early neuromyelitis optica. Ann Neurol 66: 617-629. doi:10.1002/ana.21802. PubMed: 19938104.
11. Saadoun S, Waters P, Bell A, Vincent A, Verkman AS et al. (2010) Papadopoulos MC. Intra-cerebral injection of neuromyelitis optica immunoglobulin G and human complement produces neuromyelitis optica lesions in mice. Brain 133: 349-361. doi:10.1093/brain/awp309. PubMed: 20047900.
12. Chihara N, Aranami T, Sato W, Miyazaki Y, Miyake S et al. (2011) Interleukin 6 signaling promotes anti-aquaporin 4 autoantibody production from plasmablasts in neuromyelitis optica. Proc Natl Acad Sci U S A 108: 3701-3706. doi:10.1073/pnas.1017385108. PubMed: 21321193.
13. Hoyer BF, Moser K, Hauser AE, Peddinghaus A, Voigt C et al. (2004) Short-lived plasmablasts and long-lived plasma cells contribute to chronic humoral autoimmunity in NZB/W mice. J Exp Med 199: 1577-1584. doi:10.1084/jem.20040168. PubMed: 15173206.
14. Takahashi T, Fujihara K, Nakashima I, Misu T, Miyazawa I et al. (2007) Anti-aquaporin-4 antibody is involved in the pathogenesis of NMO: a study on antibody titre. Brain 130: 1235-1243. doi:10.1093/brain/awm062. PubMed: 17449477.
15. Okada K, Matsushita T, Kira J, Tsuji S (2010) B-cell activating factor of the TNF family is upregulated in neuromyelitis optica. Neurology 74: 177-178. doi:10.1212/WNL.0b013e3181c919ee. PubMed: 20065253.
16. Uzawa A, Mori M, Arai K, Sato Y, Hayakawa S et al. (2010) Cytokine and chemokine profiles in neuromyelitis optica: significance of inyterleukin-6. Mult Scler 16: 1443-1452. doi: 10.1177/1352458510379247. PubMed: 20739337.
17. Narikawa K, Misu T, Fujihara K, Nakashima I, Sato S et al. (2004) CSF chemokine levels in relapsing neuromyelitis optica and multiple sclerosis. J Neuroimmunol 149: 182-186. doi:10.1016/j.jneuroim.2003.12.010. PubMed: 15020078.
18. Wingerchuk DM, Lennon VA, Pittock SJ, Lucchinetti CF, Weinshenker BG. (2006) (2006) Revised diagnostic criteria for neuromyelitis optica. Neurology 66: 1485-1489. doi:10.1212/01.wnl.0000216139.44259.74. PubMed: 16717206.
19. Polman CH, Reingold SC, Banwell B, Clanet M, Cohen JA et al. (2011) Diagnostic criteria for multiple sclerosis: 2010 revisions to the McDonald criteria. Ann Neurol 69: 292-302. doi:10.1002/ana.22366. PubMed: 21387374.
20. Mei HE, Yoshida T, Sime W, Hiepe F, Thiele K et al. (2009) Blood-borne human plasma cells in steady state are derived from mucosal immune responses. Blood 113: 2461-2469. doi:10.1182/blood-2008-04-153544. PubMed: 18987362.
21. Tiller T, Meffre E, Yurasov S, Tsuiji M, Nussenzweig MC et al. (2008) Efficient generation of monoclonal antibodies from single human B cells by single cell RT-PCR and expression vector cloning. J Immunol Methods 329: 112-124. doi:10.1016/j.jim.2007.09.017. PubMed: 17996249.
22. Klein U, Rajewsky K, Küppers R (1998) Human immunoglobulin (Ig)M +IgD+ peripheral blood B cells expressing the CD27 cell surface antigen carry somatically mutated variable region genes: CD27 as a general marker for somatically mutated (memory) B cells. J Exp Med 188: 1679-1689. doi:10.1084/jem.188.9.1679. PubMed: 9802980.
23. Liebersbach BF, Sanderson RD (1994) Expression of syndecan-1 inhibits cell invasion into type I collagen. J Biol Chem 269: 20013-20019. PubMed: 8051085.
24. Jacobi AM, Mei H, Hoyer BF, Mumtaz IM, Thiele K et al. (2010) HLA-DR^{high}/CD27^{high} plasmablasts indicate active disease in patients with systemic lupus erythematosus. Ann Rheum Dis 69: 305-308. doi: 10.1136/ard.2008.096495. PubMed: 19196727.
25. Wrammert J, Smith K, Miller J, Langley WA, Kokko K et al. (2008) Rapid cloning of high-affinity human monoclonal antibodies against influenza virus. Nature 453: 667-671. doi:10.1038/nature06890. PubMed: 18449194.
26. Odendahl M, Mei H, Hoyer BF, Jacobi AM, Hansen A et al. (2005) Generation of migratory antigen-specific plasma blasts and mobilization of resident plasma cells in a secondly immune response. Blood 105: 1614-1620. doi:10.1182/blood-2004-07-2507. PubMed: 15507523.
27. Manz RA, Hauser AE, Hiepe F, Radbruch A (2005) Maintenance of serum antibody levels. Annu Rev Immunol 23: 367-386. doi:10.1146/annurev.immunol.23.021704.115723. PubMed: 15771575.
28. Tiller T, Tsuiji M, Yurasov S, Velinzon K, Nussenzweig MC et al. (2007) Autoreactivity in human IgG+ memory B cells. Immunity 26: 205-213. doi:10.1016/j.immuni.2007.01.009. PubMed: 17306569.
29. Ratelade J, Bennett JL, Verkman AS (2011) Intravenous neuromyelitis optica autoantibody in mice targets aquaporin-4 in peripheral organs and area postrema. PLOS ONE 6: e27412. doi:10.1371/journal.pone.0027412. PubMed: 22076159.
30. Marques CP, Kapil P, Hinton DR, Hindinger C, Nutt SL et al. (2011) CXCR3-dependent plasma blast migration to the central nervous system during viral encephalomyelitis. J Virol 85: 6136-6147. doi: 10.1128/JVI.00202-11. PubMed: 21507985.
31. Jarius S, Paul F, Franciotta D, Ruprecht K, Ringelstein M et al. (2011) Crebrospinal fluid findings in aquaporin-4 antibody positive neuromyelitis optica: reaults from 211 lumbar punctures. J Neurol Sci 306: 82-90. doi:10.1016/j.jns.2011.03.038. PubMed: 21550068.
32. Araki M, Aranami T, Matsuoka T, Nakamura M, Miyake S et al. (2013) Clinical improvement in a patient with neuromyelitis optica following therapy with the anti-IL-6 receptor monoclonal antibody tocilizumab. Mod Rheumatol 23: 827-831. doi:10.1007/s10165-012-0715-9. PubMed: 22782533.
33. Ayzenberg I, Kleiter I, Schröder A, Hellwig K, Chan A et al. (2013) Interleukin-6 receptor blockade in neuromyelitis optica patients non-responsive to anti-CD20 therapy. JAMA Neurol 70: 394-397. doi: 10.1001/jamaneurol.2013.1246. PubMed: 23358868.
34. Jenh CH, Cox MA, Reich EP, Sullivan L, Chen SC et al. (2012) A selective and potent CXCR3 antagonist SCH 546738 attenuates the development of autoimmune diseases and delays graft rejection. BMC Immunol 13: 2. doi:10.1186/1471-2172-13-2. PubMed: 22233170.

Magnetic Resonance Imaging 31 (2013) 990–995

Contents lists available at SciVerse ScienceDirect

Magnetic Resonance Imaging

journal homepage: www.mrijournal.com

Abnormalities of cerebral blood flow in multiple sclerosis: A pseudocontinuous arterial spin labeling MRI study☆

Miho Ota [a,*], Noriko Sato [b], Yasuhiro Nakata [b], Kimiteru Ito [b], Kouhei Kamiya [b], Norihide Maikusa [c], Masafumi Ogawa [d], Tomoko Okamoto [d], Satoko Obu [a], Takamasa Noda [e], Manabu Araki [d], Takashi Yamamura [f], Hiroshi Kunugi [a]

[a] Department of Mental Disorder Research, National Institute of Neuroscience, National Center of Neurology and Psychiatry, 4-1-1, Ogawa-Higashi, Kodaira, Tokyo 187-8502, Japan
[b] Department of Radiology, National Center of Neurology and Psychiatry, 4-1-1, Ogawa-Higashi, Kodaira, Tokyo 187-8551, Japan
[c] Department of Imaging Neuroinformatics, Integrative Brain Imaging Center, National Center Hospital of Neurology and Psychiatry, 4-1-1 Ogawa-Higashi, Kodaira, Tokyo 187-8502, Japan
[d] Department of Neurology, National Center of Neurology and Psychiatry, 4-1-1, Ogawa-Higashi, Kodaira, Tokyo 187-8551, Japan
[e] Department of Psychiatry, National Center of Neurology and Psychiatry, 4-1-1, Ogawa-Higashi, Kodaira, Tokyo 187-8551, Japan
[f] Department of Immunology, National Institute of Neuroscience, National Center of Neurology and Psychiatry, 4-1-1, Ogawa-Higashi, Kodaira, Tokyo 187-8502, Japan

ARTICLE INFO

Article history:
Received 20 September 2012
Revised 30 January 2013
Accepted 9 March 2013

Keywords:
Cerebral blood flow
Multiple sclerosis
Pseudocontinuous arterial spin labeling
T2-hyperintense lesion

ABSTRACT

Arterial spin labeling (ASL) is a noninvasive technique that can measure cerebral blood flow (CBF). To our knowledge, there is no study that examined regional CBF of multiple sclerosis (MS) patients by using this technique. The present study assessed the relationship between clinical presentations and functional imaging data in MS using pseudocontinuous arterial spin labeling (pCASL). Twenty-seven patients with MS and 24 healthy volunteers underwent magnetic resonance imaging and pCASL to assess CBF. Differences in CBF between the two groups and the relationships of CBF values with the T2-hyperintense volume were evaluated. Compared to the healthy volunteers, reduced CBF was found in the bilateral thalami and right frontal region of the MS patients. The volume of the T2-hyperintense lesion was negatively correlated with regional CBF in some areas, such as both thalami. Our results suggest that demyelinated lesions in MS mainly have a remote effect on the thalamus and that the measurement of CBF using ASL could be an objective marker for monitoring disease activity in MS.

1. Introduction

Multiple sclerosis (MS) is a common autoimmune disorder of the central nervous system (CNS) characterized by inflammatory demyelination and secondary axonal degeneration. Although MS has classically been thought of as a typical white matter disorder, the involvement of gray matter regions in the demyelinating process was acknowledged in early pathology studies [1–5], and some hypotheses have been put forward that have explored possible pathogenic processes leading to gray matter damage. These processes could be either primary (arising within gray matter regions) or secondary (pathological changes in gray matter regions that result from continuing damage in the cerebral white matter) and might be intricately connected with each other [6].

Positron emission tomography (PET), single photon emission computed tomography (SPECT) and dynamic susceptibility contrast (DSC)-enhanced magnetic resonance imaging (MRI) have been used to investigate cerebral metabolic rate, cerebral blood flow (CBF) and cerebral perfusion in MS, respectively. Such imaging techniques have shown significant decreases in areas of white matter, cortical gray matter, subcortical gray matter and normal-appearing white matter [7–16]. However, due to the dissemination of MS lesions in space and time, potential markers for determining their outcomes are poorly understood.

Arterial spin labeling (ASL) MRI is a noninvasive technique that can measure CBF. ASL MRI has two major categories: continuous ASL (CASL) and pulsed ASL (PASL) [17]. The CASL technique uses continuous adiabatic inversion, whereas PASL uses a single inversion pulse. Due to the long steady-state tagging, this technique often has high power disposition and sometimes requires a second radio-frequency (RF) coil for spin labeling [18,19]. Therefore, it has not been widely used compared with PASL, which is simpler in implementation. The recently developed pseudocontinuous ASL (pCASL) MRI is an intermediate technique between CASL and PASL [20–22]. This technique uses a series of discrete RF pulses to mimic the CASL method for spin labeling and brings the potential of combining the

☆ Conflict of interest: None.

* Corresponding author. Tel.: +81 42 341 2712; fax: +81 42 346 2094.
E-mail address: ota@ncnp.go.jp (M. Ota).

0730-725X/$ – see front matter © 2013 Elsevier Inc. All rights reserved.
http://dx.doi.org/10.1016/j.mri.2013.03.016

merits of PASL, including less hardware demand and higher tagging efficiency, and CASL, which include a longer tagging bolus and thus a higher signal-to-noise ratio.

ASL measures CBF by taking advantage of arterial water as a freely diffusible tracer, avoiding the need for gadolinium or radioactive ligands; thus, ASL would be a noninvasive and repeatable method of measuring CBF. The ASL technique could be used in place of DSC, PET and SPECT for the examination of neurologic disorders.

We hypothesized that decreased CBF measured by pCASL would, in reflecting neuronal and axonal loss, be associated with the clinical course and disabling forms of MS. In the present study, we assessed the relationship between clinical presentations and functional imaging data in MS using pCASL.

2. Material and methods

2.1. Participant selection

The subjects were 27 patients with MS and 24 healthy controls matched for age, gender and whole brain volume. MS was diagnosed by using previously defined criteria [23]. One female patient out of 27 was the primary progressive MS, and 8 out of 27 (all of them were female, mean age = 47.3 ± 12.9 years) were the secondary progressive MS. No subject had a previous history of any other significant central nervous or systemic autoimmune conditions. The healthy controls were all volunteers without any confirmed neuropsychiatric or major medical illness. All MS subjects underwent a neurological examination to evaluate their Expanded Disability Status Scale (EDSS) scores [24]. The demographic and clinical data of the subjects are shown in Table 1. The study protocol was approved by the Ethics Committee of the National Center of Neurology and Psychiatry, Japan. Informed consent for participation in the study was obtained from all subjects.

2.2. MRI data acquisition and processing

Experiments were performed on a 3-T MR system (Philips Medical Systems, Best, the Netherlands). High spatial resolution, 3-dimensional (3D) T1-weighted images were used for morphometric study. 3D T1-weighted images were acquired in the sagittal plane [repetition time (TR)/echo time (TE), 7.18/3.46; flip angle, 10°; effective section thickness, 0.6 mm; slab thickness, 180 mm; matrix, 384 × 384; field of view (FOV), 261 × 261 mm; number of signals acquired, 1], yielding 300 contiguous slices through the brain. In addition to 3D T1-weighted images, we acquired axial T2-weighted turbo spin echo images (TR/TE, 4507/80; slice thickness, 3 mm; intersection gap, 1.5 mm; matrix, 640 × 640; FOV, 230 × 230 mm; number of signals acquired, 1) and axial fluid-attenuated inversion recovery (FLAIR) images (TR/TE/inversion time, 10,000/120/2650 ms; slice thickness, 3 mm; intersection gap, 1.5 mm; matrix, 512 × 512; FOV, 230 × 230 mm; number of signals acquired, 1). The imaging parameters for all of the pCASL experiments were identical: single-shot gradient-echo echo planar imaging (EPI) in combination with parallel imaging (SENSE factor 2.0), FOV = 240 × 240, matrix =64 × 64, voxel size = 3.75 × 3.75 mm, 20 slices acquired in ascending order, slice thickness = 7 mm, 1-mm gap between slices, labeling duration = 1650 ms, post spin labeling delay = 1520 ms, TR =4000 ms, TE = 12 ms, time interval between consecutive slice acquisitions = 32.0 ms, RF duration = 0.5 ms, pause between RF pulses = 0.5 ms, labeling pulse flip angle = 18°, bandwidth = 3.3 kHz/pixel, echo train length = 35. Thirty-two pairs of control/label images were acquired and averaged. The scan duration was 4:24. For measurement of the magnetization of arterial blood and also for segmentation purposes, an EPI M0 image was acquired separately with the same geometry and the same imaging parameters as the pCASL without labeling.

Table 1
Characteristics of the study sample.

	Healthy volunteers	Multiple sclerosis patients
Male/female	7/17	7/20
Age	38.3 ± 13.2	42.7 ± 13.6
Whole brain volume (L)	1.1 ± 0.1	1.1 ± 0.1
Duration of illness		10.6 ± 9.2
EDSS		4.4 ± 2.5
T2-hyperintense lesion volume (cm^3)		3.4 ± 4.0

2.3. Postprocessing of the ASL data

Because pCASL and M0 images were acquired separately, both image signal intensities were corrected for data scaling. Corrected data were transferred to a workstation and analyzed using ASLtbx software working on Matlab (Math Works, Natick, MA, USA) [25]. For the CBF calculations, we added the attenuation correction for the transversal relaxation rate of gray matter to the original equation as shown:

$$\begin{aligned}\text{CBF (ml/100 g/min)} &= (6000 * \text{delM} * \text{lamb}) \\ &* \exp(\text{TE}/T^*_{2.\text{gm}}/[2 * \text{alp} * T_{1,\text{blood}} * \text{M0WM}\{\exp(-w/T_{1,\text{blood}}) \\ &-\exp\left(-(\text{tau}+w)/T_{1,\text{blood}}\right)\}],\end{aligned}$$

Where delM is the difference signal between the control and label acquisitions, lamb is the blood/tissue water partition coefficient, $T_{1,\text{blood}}$ is the longitudinal relaxation time of blood, tau is the labeling time, w is the post labeling delay time, TE is the echo time and $T^*_{2.\text{gm}}$ is the transversal relaxation time of gray matter (assumed to be 44.2 ms) [26]. Alp is the labeling efficiency, and M0WM is the average intensity in the control image within the white matter that was derived from the segmented M0 white matter image calculated using Statistical Parametric Mapping 5 software (SPM5; Wellcome Department of Imaging Neuroscience, London, UK) running on Matlab 7.0. The parameters used in this study were alp = 0.85 (assumed) [17], $T_{1,\text{blood}}$ = 1664 ms (assumed) [27], λ = 0.9 g/ml (assumed) [28], tau = 1.65 s (calculated) and w = 1525 (calculated) ms.

The mean CBF image derived using the ASLtbx software contained some spike noise, and thus, a median filter (a nonlinear digital filtering technique) was used in this study. In median filtering, the neighboring pixels are ranked according to the intensity, and the median value becomes the new value for the central pixel. Since the slice gap that we used was somewhat large, simple 2D median filtering was used. Fig. 1 illustrated the image from the ASL sequence in a single subject. To evaluate CBF voxel-basically, mean CBF images were normalized to the standard space. On the occasion of normalization, each individual 3D-T1 image was first coregistered and resliced to its own M0 image. Next, the coregistered 3D-T1 image was normalized to the "avg152T1" image regarded as the anatomically standard image in SPM5, and then the transformation matrix was applied to the FA maps to normalize them to the standard space. The spatially normalized images were resliced with a final voxel size of approximately 4 × 4 × 8 mm^3. Each map was then spatially smoothed with a 4-mm full-width at half-maximum Gaussian kernel in order to decrease spatial noise and compensate for the inexactitude of normalization.

2.4. Measure of volume of T2-hyperintense lesion

The T2-weighted data and FLAIR images for each subject were transferred to the workstation. To measure the accurate volume of the T2-hyperintense lesion, individual T2-weighted data and FLAIR

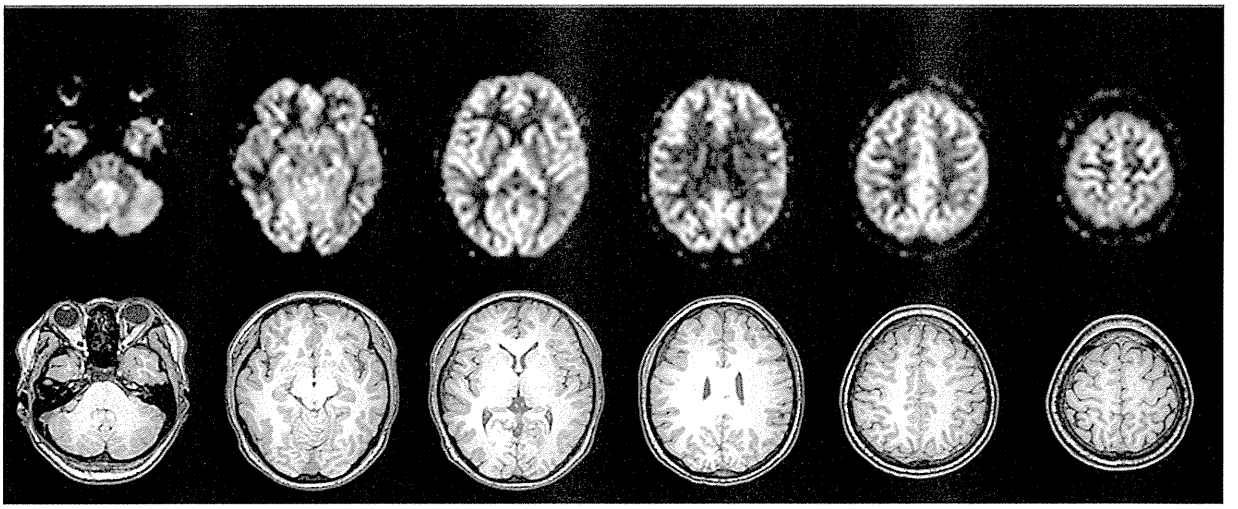

Fig. 1. The upper row showed the typical example of ASL CBF maps acquired in a single healthy volunteer, and lower row showed corresponding slices of T1-weighted image.

data sets were analyzed using QBrain@1.1 [22]. The volume quantifications were first performed with manual segmentation and second with the fully automatic segmentation algorithms. Using the software, the T2-hyperintense lesions can be reliably quantified in the milliliter range.

2.5. Measure of whole brain volume

We regarded the gray matter volume plus white matter volume as the whole brain volume. The values of gray and white matter volumes of individual subjects were extracted with the Easy Volume toolbox [29] running on Matlab 7.0. The gray matter and white matter volume images were derived from the segmented 3D-T1 image calculated using SPM5.

2.6. Statistical analysis

We first evaluated the correlations among the EDSS score, age, duration of illness and the ratio of T2-hyperintense lesion volume/whole brain volume in the MS patients by using Pearson's correlation analysis. Statistical analyses were performed using SPSS Statistics for Windows 17.0 software (SPSS, Tokyo, Japan).

Next, statistical analyses for the CBF were performed using SPM5 software. We evaluated the difference in regional CBF (rCBF) between the MS patients and healthy subjects using age and gender as nuisance variables. Only correlations that met the following criteria were deemed statistically significant: seed levels of $P < .05$ [false discovery rate (FDR) corrected] and a cluster level of $P < .05$ (uncorrected).

Next, correlations between rCBF values and the ratio of T2-hyperintense lesion volume/whole brain volume and between rCBF values and EDSS scores were assessed using age, gender and duration of illness as nuisance variables. Only correlations that met the following criteria were deemed significant: a seed level of $P < .001$ (uncorrected) and a cluster level of $P < .05$ (uncorrected).

Finally, we highlighted the influence of the T2-hyperintense lesion on the CBF. We masked the latter results with the regions for which the results of the former analysis were regarded as significant.

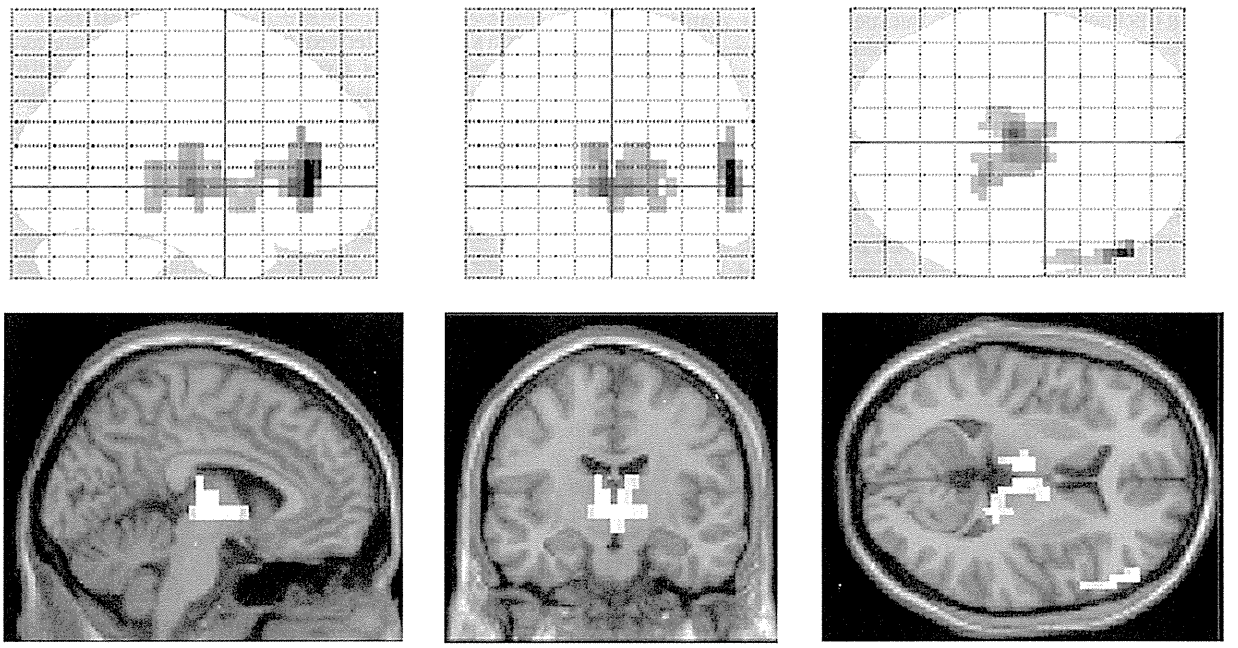

Fig. 2. There were significant reductions of CBF in the right prefrontal cortex and bilateral thalami in the MS patients compared to the healthy controls [$P < .05$ (FDR corrected)].

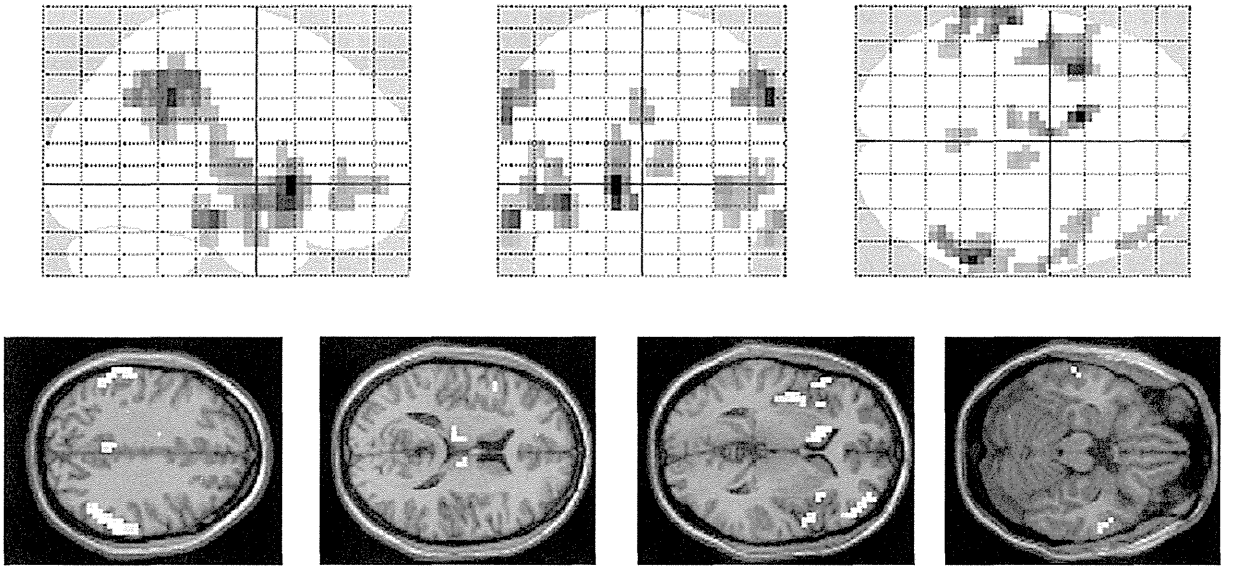

Fig. 3. There were negative correlations between the T2-hyperintense lesion volume/whole brain volume ratio and the regional CBF values in several areas throughout the brain in the MS patients ($P < .001$, uncorrected).

This mask was based on partially the same data of the latter analysis; there existed a multiple testing problem. So, we use the formal thresholding (e.g., FDR) that accounts for this multiplicity [30]. The mask applied the seed levels of $P < .05$ (FDR corrected) as statistically significant.

3. Results

There were no significant correlations between any combinations of two factors of EDSS score, age, duration of illness and the ratio of T2-hyperintense lesion volume/whole brain volume in the MS patients (data not shown). There were significant reductions of CBF in the bilateral thalami and right frontal region of the MS patients compared to the healthy controls (Fig. 2 and Table 2).

There was no increase of CBF in MS patients (data not shown). In the MS patient group, the T2-hyperintense lesion volume/whole brain volume ratio was negatively correlated with rCBF values in the right frontal region, both parietal and temporal regions, both insulae, the left caudate, both thalami and both posterior cinguli (Fig. 3 and Table 3). There were no differences of regional CBF between relapsing–remitting MS patients and secondary progressive MS patients (data not shown).

In contrast, there was no correlation between the EDSS scores and rCBF values (data not shown). There were significant negative correlations between the ratio of the T2-hyperintense lesion volume to whole brain volume and CBF in both thalami when we masked the second results with the regions in which the results of the first analysis were regarded as significant (Fig. 4).

4. Discussion

To our knowledge, this is the first evaluation of the possible relationships between clinical presentations of MS and CBF using pCASL. By using the pCASL technique, we found significant correlations between the volume of T2-hyperintense lesions and the rCBF values. In particular, CBF in the thalamus was significantly decreased in the patients with MS compared to that of the healthy subjects, and thalamic CBF was correlated with the volume of T2-hyperintense lesion.

There were a few studies of MS using CASL and PASL [14,31]. One study using the CASL showed the reduction of thalamic CBF in MS; however, they did not evaluate the correlation between the volume of T2-hyperintense lesions and the rCBF values [14]. On the other hand, the study using PASL showed not the correlation between them but the correlation between the volume of lesions and mean cortical CBF [31]. These facts may indicate that the CBF study using pCASL calculates the rigorous CBF value. In addition, these studies, including our study, did not show the correlation between the EDSS and rCBF. This may result from the fact that the EDSS mainly focused on the ambulatory ability, not on the higher brain function, so the change of

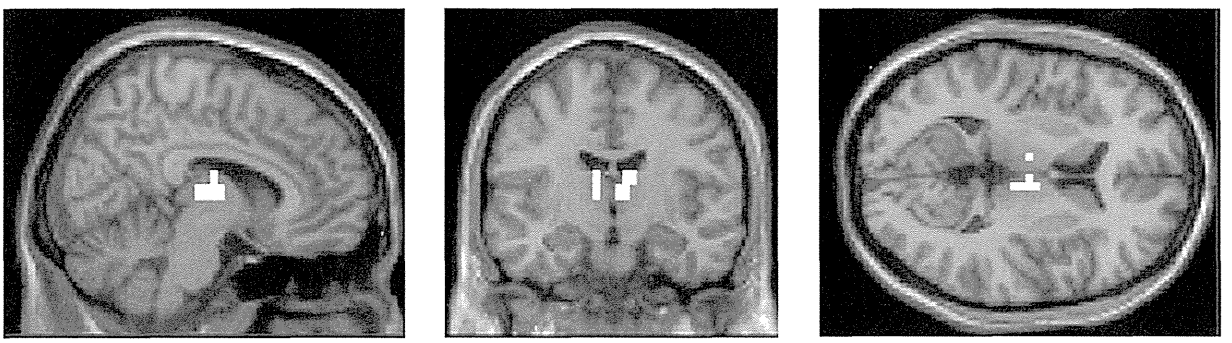

Fig. 4. When the correlation analysis was restricted in both thalami where the CBF reduction was detected in the MS patients, there were significant negative correlations between the T2-hyperintense lesion volume/whole brain volume ratio and the CBF values.

cortical CBF in MS did not reflect the EDSS score. In recent years, the MS Functional Composite (MSFC) was proposed for a new multidimensional clinical outcome measure of MS [32]. The MSFC comprises quantitative functional measures of three key clinical dimensions of MS: leg function ambulation, arm/hand function and cognitive function. Further studies with information on MSFC are necessary to address this issue. Additionally, we showed the CBF reduction of the patients with MS in the inferior prefrontal cortex. Previous study showed that MS patients with long duration of disease showed atrophy of the thalami and inferior frontal gyrus [33]. The participants in this study showed relatively long disease duration (Table 1); then the CBF of the patients would show the reduction.

We also found negative correlations between the ratio of the T2-hyperintense lesion volume/whole brain volume and regional CBF in several areas throughout the brain in the MS patients. We focused on volume and not on distribution of the T2-hyperintense lesion in the whole brain, and therefore, the relationship between the volume of lesion and the regional CBF was not examined. However, some previous studies showed reduced metabolism in the prefrontal, parietal and occipital cortex and hippocampus, thalamus, putamen and caudate in MS [7,8,13,14], and those findings are compatible with our results.

Regarding the thalamus, an MRI study of MS patients reported a decrease in thalamic volume and *N*-acetyl aspartate [34]. Those authors also identified the thalamic neuronal loss in MS patients by postmortem examination. Evaluations of the metabolism and perfusion in the brains of patients with MS have also revealed hypometabolism and hypoperfusion in the thalamus [9,12,14] Furthermore, PET metabolic studies suggest a possible correlation between thalamic hypometabolism and cognitive impairment [7], memory disturbance [13] and the volume of deep white matter lesions [8]. The decreased thalamic CBF observed in our study is consistent with the findings of these previous studies. Another study using diffusion tensor imaging revealed the fine neural networks in the CNS [35]. The thalamus is regarded as the central relay station of the brain, and the reciprocal influence between the thalamus and its associated areas has been well described [36]. The decreased CBF that we observed in the thalamus of the MS patients may be an indication of a disconnection between cortical regions and subcortical relay systems due to the lesion process in MS.

There were some limitations of this study. First, we dealt with the whole brain CBF images, including the gray matter and white matter, voxel-basically. However, we could not detect the white matter CBF change. Previous study showed that the female patients with MS showed the change of white matter compared with men, while gender did not impact gray matter atrophy [33]. Along with the dissemination of MS lesions in space and time, co-gender participants may influence on our results. Further work with single-gender MS patients will be necessary to confirm our results. Second, we did not classify the participants into the three subgroups of MS. The subgroups of MS were defined by the clinical course of illness, and this is not for a cross-sectional study containing the first episode of illness. Not only our study but also two previous cross-sectional studies using ASL also did not show the differences among the subgroups of MS [14,31]. Further longitudinal work would show the difference among the subgroups. A third limitation of the present study is that we did not eliminate the effect of immunomodulating treatment on CBF. Further work with drug-free MS patients will be necessary to confirm our results.

In conclusion, our findings indicate that the noninvasive pCASL is a useful technique which demonstrated that regional CBF values are closely related to the brain lesions in MS. In addition, our results suggest that the demyelinating lesions in MS mainly have a remote effect on the function of the thalamus. Measurement of CBF by pCASL MRI has the potential to be an objective marker for monitoring disease activity in MS (Tables 2 and 3).

Table 2
Regions that showed significant differences in cerebral blood flow between the patients with multiple sclerosis ($n = 27$) and healthy controls ($n = 24$) using age and gender as nuisance variables.

Cluster size	*Z* score	*x*	*y*	*z*	Brain region
35	5.17	56	40	8	Right frontal lobe
114	4.61	−4	−16	0	Left thalamus
	4	8	−16	0	Right thalamus

Table 3
Regions of significant negative correlations between cerebral blood flow and T2-hyperintense lesion volume in MS patients using age, gender and duration of illness as nuisance variables.

Cluster size	*Z* score	*x*	*y*	*z*	Brain region
16	3.62	40	56	0	Right frontal lobe
35	3.98	−64	−44	32	Left parietal lobe
49	4.33	60	−40	40	Right parietal lobe
11	4.17	−60	−20	−16	Left temporal lobe
9	3.61	64	−4	−16	Right temporal lobe
68	4.29	−36	16	−8	Left insula
24	3.59	56	8	0	Right insula
23	4.59	−12	16	0	Left caudate
11	3.55	−12	−8	8	Left thalamus
9	3.42	8	−16	8	Right thalamus
12	3.37	4	−48	32	Right posterior cingulate
	3.33	−4	−44	40	Left posterior cingulate

Acknowledgments

We are grateful to Ms. Yuriko Suzuki at Philips for helpful discussions. This study was supported by Health and Labour Sciences Research Grants (Comprehensive Research on Disability, Health, and Welfare, #H23-seisin-young scientist 013; #H21-kokoro-002), an Intramural Research Grant for Neurological and Psychiatric Disorders of NCNP and "Understanding of molecular and environmental bases for brain health" carried out under the Strategic Research Program for Brain Sciences of the Ministry of Education, Culture, Sports, Science and Technology of Japan.

References

[1] Brownell B, Hughes JT. The distribution of plaques in the cerebrum in multiple sclerosis. J Neurol Neurosurg Psychiatry 1962;25:315-20.
[2] Dawson JW. The histology of multiple sclerosis. Trans R Soc (Edinb) 1916;50:517-740.
[3] Dinkler M. Zur Kasuistik der multiplen Herdsklerose des Gehirns und Ruckenmarks. Deuts Zeits f Nervenheilk 1904;26:233-47.
[4] Sander M. Hirnrindenbefunde bei multipler Sklerose. Monatschrift Psychiatrie Neurol 1898;IV:427-36.
[5] Schob F. Ein Beitrag zur pathologischen Anatomie der multiplen Sklerose. Monatschrift Psychiatrie Neurol 1907;22:62-87.
[6] Geurts JJ, Barkhof F. Grey matter pathology in multiple sclerosis. Lancet Neurol 2008;7:841-51.
[7] Blinkenberg M, Rune K, Jensen CV, Ravnborg M, Kyllingsbaek S, Holm S, et al. Cortical cerebral metabolism correlates with MRI lesion load and cognitive dysfunction in MS. Neurology 2000;54:558-64.
[8] Derache N, Marié RM, Constans JM, Defer GL. Reduced thalamic and cerebellar rest metabolism in relapsing-remitting multiple sclerosis, a positron emission tomography study: correlations to lesion load. J Neurol Sci 2006;245:103-9.
[9] Inglese M, Park SJ, Johnson G, Babb JS, Miles L, Jaggi H, et al. Deep gray matter perfusion in multiple sclerosis: dynamic susceptibility contrast perfusion magnetic resonance imaging at 3 T. Arch Neurol 2007;64:196-202.
[10] Law M, Saindane AM, Ge Y, Babb JS, Johnson G, Mannon LJ, et al. Microvascular abnormality in relapsing-remitting multiple sclerosis: perfusion MR imaging findings in normal-appearing white matter. Radiology 2004;231:645-52.
[11] Lycke J, Wikkelsö C, Bergh AC, Jacobsson L, Andersen O. Regional cerebral blood flow in multiple sclerosis measured by single photon emission tomography with technetium-99 m hexamethylpropyleneamine oxime. Eur Neurol 1993;33:163-7.

[12] Papadaki EZ, Mastorodemos VC, Amanakis EZ, Tsekouras KC, Papadakis AE, Tsavalas ND, et al. White matter and deep gray matter hemodynamic changes in multiple sclerosis patients with clinically isolated syndrome. Magn Reson Med 2012;68:1932-42.
[13] Paulesu E, Perani D, Fazio F, Comi G, Pozzilli C, Martinelli V, et al. Functional basis of memory impairment in multiple sclerosis: a [18 F]FDG PET study. Neuroimage 1996;4:87-96.
[14] Rashid W, Parkes LM, Ingle GT, Chard DT, Toosy AT, Altmann DR, et al. Abnormalities of cerebral perfusion in multiple sclerosis. J Neurol Neurosurg Psychiatry 2004;75:1288-93.
[15] Saindane AM, Law M, Ge Y, Johnson G, Babb JS, Grossman RI. Correlation of diffusion tensor and dynamic perfusion MR imaging metrics in normal-appearing corpus callosum: support for primary hypoperfusion in multiple sclerosis. AJNR Am J Neuroradiol 2007;28:767-72.
[16] Varga AW, Johnson G, Babb JS, Herbert J, Grossman RI, Inglese M. White matter hemodynamic abnormalities precede sub-cortical gray matter changes in multiple sclerosis. J Neurol Sci 2009;282:28-33.
[17] Aslan S, Xu F, Wang PL, Uh J, Yezhuvath US, van Osch M, et al. Estimation of labeling efficiency in pseudocontinuous arterial spin labeling. Magn Reson Med 2010;63:765-71.
[18] Wolff SD, Balaban RS. Magnetization transfer contrast (MTC) and tissue water proton relaxation in vivo. Magn Reson Med 1989;10:135-44.
[19] Detre JA, Alsop DC. Perfusion magnetic resonance imaging with continuous arterial spin labeling: methods and clinical applications in the central nervous system. Eur J Radiol 1999;30:115-24.
[20] Dai W, Garcia D, de Bazelaire C, Alsop DC. Continuous flow-driven inversion for arterial spin labeling using pulsed radio frequency and gradient fields. Magn Reson Med 2008;60:1488-97.
[21] Wong EC. Vessel-encoded arterial spin-labeling using pseudocontinuous tagging. Magn Reson Med 2007;58:1086-91.
[22] Wu WC, Fernandez-Seara M, Detre JA, Wehrli FW, Wang J. A theoretical and experimental investigation of the tagging efficiency of pseudocontinuous arterial spin labeling. Magn Reson Med 2007;58:1020-7.
[23] Polman CH, Reingold SC, Banwell B, Clanet M, Cohen JA, Filippi M, et al. Diagnostic criteria for multiple sclerosis: 2010 revisions to the McDonald criteria. Ann Neurol 2011;69:292-302.
[24] Kurtzke JF. Rating neurologic impairment in multiple sclerosis: an expanded disability status scale (EDSS). Neurology 1983;33:1444-52.
[25] Wang Z, Aguirre GK, Rao H, Wang J, Fernández-Seara MA, Childress AR, et al. Empirical optimization of ASL data analysis using an ASL data processing toolbox: ASLtbx. Magn Reson Imaging 2008;26:261-9.
[26] Cavuşoğlu M, Pfeuffer J, Uğurbil K, Uludağ K. Comparison of pulsed arterial spin labeling encoding schemes and absolute perfusion quantification. Magn Reson Imaging 2009;27:1039-45.
[27] Lu H, Clingman C, Golay X, van Zijl PC. Determining the longitudinal relaxation time (T1) of blood at 3.0 tesla. Magn Reson Med 2004;52:679-82.
[28] Wang J, Zhang Y, Wolf RL, Roc AC, Alsop DC, Detre JA. Amplitude-modulated continuous arterial spin-labeling 3.0-T perfusion MR imaging with a single coil: feasibility study. Radiology 2005;235:218-28.
[29] Pernet C, Andersson J, Paulesu E, Demonet JF. When all hypotheses are right: a multifocal account of dyslexia. Hum Brain Mapp 2009;30:2278-92.
[30] Carter CS, Heckers S, Nichols T, Pine DS, Strother S. Optimizing the design and analysis of clinical functional magnetic resonance imaging research studies. Biol Psychiatry 2008;64:842-9.
[31] Amann M, Achtnichts L, Hirsch JG, Naegelin Y, Gregori J, Weier K, et al. 3D GRASE arterial spin labelling reveals an inverse correlation of cortical perfusion with the white matter lesion volume in MS. Mult Scler 2012;18:1570-6.
[32] Fischer JS, Rudick RA, Cutter GR, Reingold SC. The Multiple Sclerosis Functional Composite Measure (MSFC): an integrated approach to MS clinical outcome assessment. National MS Society Clinical Outcomes Assessment Task Force. Mult Scler 1999;5:244-50.
[33] Riccitelli G, Rocca MA, Pagani E, Martinelli V, Radaelli M, Falini A, et al. Mapping regional grey and white matter atrophy in relapsing-remitting multiple sclerosis. Mult Scler 2012;18:1027-37.
[34] Cifelli A, Arridge M, Jezzard P, Esiri MM, Palace J, Matthews PM. Thalamic neurodegeneration in multiple sclerosis. Ann Neurol 2002;52:650-3.
[35] Behrens TE, Johansen-Berg H, Woolrich MW, Smith SM, Wheeler-Kingshott CA, Boulby PA, et al. Noninvasive mapping of connections between human thalamus and cortex using diffusion imaging. Nat Neurosci 2003;6:750-7.
[36] Buffon F, Molko N, Hervé D, Porcher R, Denghien I, Pappata S, et al. Longitudinal diffusion changes in cerebral hemispheres after MCA infarcts. J Cereb Blood Flow Metab 2005;25:641-50.

PLOS ONE

Nuclear Receptor NR4A2 Orchestrates Th17 Cell-Mediated Autoimmune Inflammation via IL-21 Signalling

Ben J. E. Raveney, Shinji Oki[9], Takashi Yamamura*[9]

Department of Immunology, National Institute of Neuroscience, National Center of Neurology and Psychiatry, Kodaira, Tokyo, Japan

Abstract

IL-17-producing $CD4^+$ T helper 17 (Th17) cells are pathogenic in a range of human autoimmune diseases and corresponding animal models. We now demonstrate that such T cells infiltrating the target organ during the induction of experimental autoimmune encephalomyelitis (EAE) and experimental autoimmune uveoretinitis (EAU) specifically express NR4A2. Further, we reveal a critical involvement of NR4A2 in Th17 cell functions and Th17 cell-driven autoimmune diseases. When NR4A2 expression was blocked with siRNA, full Th17 differentiation was prevented *in vitro*: although cells expressed the master Th17 regulator, RORγt, they expressed reduced levels of IL-23R and were unable to produce IL-17 and IL-21. Notably, Th17 differentiation in the absence of NR4A2 was restored by exogenous IL-21, indicating that NR4A2 controls full maturation of Th17 cells via autocrine IL-21 signalling. Preventing NR4A2 expression *in vivo* by systemic treatment with NR4A2-specific siRNA also reduced Th17 effector responses and furthermore protected mice from EAE induction. In addition, the lack of disease was associated with a reduction in autocrine IL-21 production and IL-23R expression. Similar modulation of NR4A2 expression was also effective as an intervention, reversing established autoimmune responses and ameliorating clinical disease symptoms. Thus, NR4A2 appears to control Th17 differentiation and so plays an essential role in the development of Th17-mediated autoimmune disease. As NR4A2 is also upregulated during human autoimmune disease, targeting NR4A2 may provide a new therapeutic approach in treating autoimmune disease.

Citation: Raveney BJE, Oki S, Yamamura T (2013) Nuclear Receptor NR4A2 Orchestrates Th17 Cell-Mediated Autoimmune Inflammation via IL-21 Signalling. PLoS ONE 8(2): e56595. doi:10.1371/journal.pone.0056595

Editor: Martin Stangel, Hannover Medical School, Germany

Received September 5, 2012; **Accepted** January 11, 2013; **Published** February 21, 2013

Funding: This work was supported by the grants from the Ministry of Health, Labour, and Welfare of Japan, the Council for Science and Technology Policy (CSTP) and the Ministry of Education, Science, Culture, Sports, and Technology of Japan. TY is a recipient of a JSPS Grant-in-Aid for Scientific Research (KAKENHI) No. 18109009, SO is a recipient of a JSPS KAKENHI Grant No. 21590087, and BJER was a recipient of a JSPS Postdoctoral Fellowship for Foreign Researchers No. P08517. The funders had no role in study design, data collection and analysis, decision to publish, or preparation of the manuscript.

Competing Interests: The authors have declared that no competing interests exist.

* E-mail: yamamura@ncnp.go.jp

[9] These authors contributed equally to this work.

Introduction

T helper (Th) cells responding to self-antigens generate pathogenic inflammatory responses in target organs, leading to local damage and so generate organ-specific autoimmune diseases. It was previously thought that $CD4^+$ interferon (IFN)-γ-secreting Th1 cells were critical in inducing autoimmune damage to the central nervous system (CNS) in human multiple sclerosis (MS) and its animal model, experimental autoimmune encephalomyelitis (EAE) [1]. However, the discovery of pathogenic IL-17-secreting Th17 cells as a separate cell lineage opened the door to new research directions towards understanding the development of autoimmune inflammation [2–4]. It is now understood that both Th1 and Th17 cells mediate autoimmune responses in rodents [5–8] as well as in humans [9,10]. Regarding the development of EAE, it has recently been proposed that the major proportion of T cells producing inflammatory cytokines, including IFN-γ, may in fact be T cells that had previously produced IL-17 [11]. Thus, manipulation of Th17 cells might prove effective in controlling complex autoimmune disease processes involving both Th1 and Th17 cells.

Naïve $CD4^+$ T cells differentiate into Th1 cells under the influence of IL-12, whereas TGF-β in combination with IL-6 is appreciated as the classical Th17-differentiating cytokine milieu [12,13]. Recently, however, Th17 differentiation pathways that do not depend on IL-6 or TGF-β have also been described [14–16]. In contrast, *in vivo* studies demonstrate that IL-23 plays a critical role in promoting generation of Th17 cells. Indeed, Th17-mediated autoimmune disease is greatly reduced or prevented in the absence of IL-23 signalling [17,18].

NR4A2, also known as Nurr1, is an orphan nuclear receptor [19–22], and its function in dopaminergic neuron signalling has been widely known. Increasing evidence suggests the role of NR4A2 in inflammatory responses during arthritis and psoriasis [23,24], and NR4A2 may also serve as a regulatory element for reducing immune-mediated tissue damage [25]. We have previously reported that NR4A2 is among the genes expressed by circulating T cells that are highly upregulated in patients with multiple sclerosis (MS) and that NR4A2 is also induced in T cells during rodent EAE [26,27]. We also demonstrated that forced NR4A2 expression enhanced non-specific production of Th1 and Th17 cytokines although further confirmation was needed to confirm the role of NR4A2 in T cell functions.

In this study, we firstly show that NR4A2 is strikingly upregulated by IL-17-secreting Th17 cells infiltrating the target organ of EAE and experimental autoimmune uveoretinitis (EAU), the murine model of posterior uveitis. Using siRNA knockdown techniques, we demonstrate that NR4A2 is dispensable for

induction of the Th17 cell transcription factor RORγt in T cells, but is critically required for the *in vitro* generation of fully functional Th17 cells capable of producing IL-17 and IL-21, and expressing the IL-23 receptor (IL-23R). Notably, addition of exogenous IL-21 was able to circumvent the requirement for NR4A2 in Th17 differentiation, and restore the expression of IL-23R and IL-17. Furthermore, NR4A2 knockdown *in vivo* by injection of NR4A2 siRNA either before or after the onset of CNS infiltration ameliorated EAE. Taken together, these data suggest that T cell NR4A2 expression is a hallmark of Th17 cell-mediated pathology and show for the first time that systemic injection of a NR4A2-targeting drug may be a treatment option for Th17-cell mediated diseases.

Materials and Methods

Animals and EAE/EAU Induction

Female C57BL/6J mice (CLEA Laboratory Animal Corp., Tokyo, Japan) aged 8–10 weeks were maintained in specific pathogen–free conditions in accordance with institutional guidelines. This study and all protocols used were approval by the Committee for Small Animal Research and Animal Welfare (National Center of Neurology and Psychiatry). Procedures were carried out under institutional guidelines and all efforts were made to minimize animal suffering. For EAE induction, mice were injected subcutaneously with 100 μg MOG_{35-55} peptide (synthesized by Toray Research Center, Tokyo, Japan) and 1 mg heat-killed mycobacterium tuberculosis H37RA emulsified in complete Freund's adjuvant (Difco, KS, USA). 200 ng Pertussis toxin (List Biological Laboratories, USA) was injected intraperitoneally (*i.p.*) on days 0 and 2 after immunization. EAE was clinically scored daily (0, no clinical signs; 1, partial tail paralysis; 2, flaccid tail; 3, partial hind limb paralysis; 4, total hind limb paralysis; 5, hind and fore leg paralysis) [28]. EAU was induced as previously described by immunization with 500 μg human interphotoreceptor binding protein $(IRBP)_{1-20}$ peptide (synthesized by Toray Research Center) in CFA per mouse plus 1 μg Pertussis toxin [29]. EAU disease severity was monitored by enumeration of the retinal-infiltrating cell number as previously described [30]. Diabetes was induced as previously described [31] by 5 daily *i.p.* doses of 40 mg/kg streptozotocin (STZ; Sigma, Tokyo, Japan) and the urine glucose level was determined daily with Diastix (Bayer, Tokyo, Japan).

siRNA Treatment

NR4A2-specifc siRNA (sense – GGACAGCAGUCCUC-CAUUAAUU, anti-sense - UUAAUGGAGGACUGCUGUC-CUU) and matching scrambled control sequence siRNA were synthesized by Takara (Shiga, Japan) or Koken (Tokyo, Japan). siRNA was transfected into cells using a mouse CD4 nucleofector kit with an Amaxa electroporator (Lonza, Basel, Switzerland) according to the manufacturer's instructions. For systemic *in vivo* administration, siRNA was stabilized in atelocollagen using an AteloGene kit according to the manufacturer's instructions (Koken) and 10 μg siRNA per mouse was injected intravenously.

Cell Isolation and Purification

Single cell splenocyte and lymph node cell suspensions were generated by mechanical disruption of tissues. CNS-infiltrating lymphocytes were isolated from spinal cords and brains as previously described [28]. Briefly, tissue was cut into small pieces and digested for 40 minutes at 37°C in RPMI 1640 media (Invitrogen, Tokyo, Japan) supplemented with 1.4 mg/ml Collagenase H and 100 μg/ml DNase I (Roche, Tokyo, Japan). Resulting tissue homogenates were forced through a 70 μm cell strainer and leukocytes were enriched using a discontinuous 37%/70% percoll density gradient centrifugation (GE Healthcare Life Sciences, Tokyo, Japan). Retinal-infiltrating cells and pancreatic-infiltrating cells were isolated by enzymatic digestion as previously described [32,33].

T cells were purified using a CD4 T cell MACS isolation kit with an AutoMACS separator according to the manufacturer's instructions (Miltenyi Biotech, Bergisch Gladbach, Germany). Where required, naïve $CD4^+CD44^-CD25^-CD62L^{high}$ T cells or memory $CD4^+CD44^+CD25^-CD62L^{low}$ T cells were further sorted using a FACS ARIA (BD Cytometry Systems, NJ, USA). For sorting of live cytokine-secreting cells, cytokine secretion assay kits (Miltenyi Biotech) were used according to the manufacturer's instructions. Briefly, cells were restimulated with 5 ng/ml PMA +500 ng/ml ionomycin (both Sigma-Aldrich, Tokyo, Japan) and anti-IL-17 and anti-IFN-γ capture antibodies were added for the final 45 minutes of culture. Secondary fluorochrome-conjugated antibodies were added to visualize captured cytokines and cells were sorted using a FACS ARIA flow cytometer.

Cell Culture

Culture media was DMEM supplemented with 10% FCS, 2 mM L-glutamine, 100 U/ml penicillin-streptomycin, and 50 μM 2-Mercaptoethanol (all Invitrogen). Where indicated, cells were activated with 2 μg/ml immobilized CD3-specific mAb (2C-11) and 1 μg/ml CD28-specific mAb (BD Pharmingen, Tokyo, Japan). Polarizing conditions were as follows: Th1, +10 ng/ml IL-12 (PeproTech, London, UK) and 10 μg/ml IL-4-specific mAb (HB188); Th17, 3 ng/ml TGF-β (R & D Systems, Minneapolis, USA), 20 ng/ml IL-6 (PeproTech), 20 ng/ml IL-23 (R & D Systems), 10 μg/ml IFN-γ-specific mAb, and 10 μg/ml IL-4-specific mAb.

Assessment of Cell Function

Cytokine concentrations in supernatants were measured by ELISA as follows: IL-17 using a mouse IL-17 DuoSet (R&D Systems), IL-21 using an IL-21 MaxLegend kit (Biolegend, San Diego, USA), and IFN-γ using a mouse IFN-γ ELISA antibody pair (BD Biosciences). Other cytokines were assessed using a FlowCytomix cytometric bead array (Bender MedSystems, Vienna, Austria) according to the manufacturer's instructions. Proliferation was determined by incubation with [^{3}H]-thymidine (1 μCi/well) for the final 12 hours of culture and incorporation of radioactivity was assessed with a β-1205 counter (Pharmacia Biotech, Freiburg, Germany). For intracellular staining, cells were restimulated with 5 ng/ml PMA +500 ng/ml ionomycin (both Sigma-Aldrich) in the presence of Golgi Stop (BD Biosciences) for 5 hours, before surface staining and fixing/intracellular staining using a Foxp3 staining kit (eBioscience, San Diego, CA, USA) according to the manufacturer's instructions. Antibodies were sourced from BioLegend (San Diego, USA), except for anti-cytoplasmic IL-23R (Millipore, Tokyo, Japan).

RNA Extraction and Quantitative RT-PCR

Total RNA was extracted from cell populations using an RNeasy Mini Kit or FastLane kit (Qiagen, Maryland, USA) according to the manufacturer's instructions. cDNA was prepared using a first-strand cDNA Kit (Takara). Quantitative real time PCR was performed with a Light Cycler-FastStart DNA Master SYBR Green I kit using a LightCycler instrument (Roche Diagnostics, Tokyo, Japan) or with a Power SYBR green master

mix using an ABI 7300 real time PCR instrument (Applied Biosystems, Warrington, UK). Primers used were as follows: GAPDH, forward AACGACCCCTTCATTGAC, reverse TCCACATACTCAGCAC; RORγt, forward TGTCCTGGGCTACCCTACTG, reverse GTGCAGGAGTAGGCCACATT; t-bet, forward GCCAGGGAACCGCTTATATG, reverse GACGATCATCTGGGTCACATTGT; IL-21, forward TCATCATTGACCTCGTGGCCC, reverse ATCGTACTTCCACTTGCAATCCC; IL-23R, forward TCAGTGCTACAATCTTCAGAGGACAT, reverse GATGGCCAAGAAGACCATTCC; IL-17A, forward ATCCCTCAAAGCTCAGCGTGTC, reverse GGGTCTTCATTGCGGTGGAGAG; and Foxp3, forward TTCTCACAACAAGGCCACTTG, reverse CCCAGGAAAGACAGCAACCCT. Gene expression values were normalized to the expression of the GAPDH housekeeping gene.

Statistical Analyses

Statistical significance of differences was tested using a Mann Whitney U test unless otherwise stated. $p<0.05$ was considered significant.

Results

Organ-specific Autoimmune Diseases EAE and EAU Accompany NR4A2 Regulation in T cells

We previously reported T cell expression of NR4A2 during EAE [27]. Here we tested whether or not NR4A2 overexpression is common to T cells involved in autoimmune diseases. We detected NR4A2 upregulation amongst T cells during the development of EAE and EAU, a Th1/Th17-mediated autoimmune disease of the retina: T cell expression of NR4A2 was observed from the earliest stages of both EAE and EAU in $CD4^+$ T cell infiltrates in the target organ and, as well as a later NR4A2 upregulation amongst circulating blood $CD4^+$ T cells (Fig. 1A&B) after the peak of clinical disease (Fig. S1A&B). Although T cells from secondary lymphoid tissue have the potential to induce EAE or EAU when they are adoptively transferred after being stimulated *in vitro* [34], no significant NR4A2 expression was detected amongst lymph node or splenic T cells at any time examined.

NR4A2 Expression is Associated with IL-17 Producing T cells in EAE

We previously observed that forced expression of NR4A2 in T cells could enhance production of both IL-17 and IFN-γ [27]. However, since this observation was made under non-physiological conditions, we attempted to verify if this finding had physiological meaning *in vivo*. Using a cytokine secretion assay, we separated populations of live $CD4^+$ T cells from the blood and CNS of EAE mice based on their production of IFN-γ and IL-17 and measured the expression levels of NR4A2 in each population. Strikingly, in the early phase of EAE, NR4A2 transcripts were detected in those T cells that produced IL-17, either alone or in combination with IFN-γ (Fig. 1C), but not in those that produced IFN-γ alone or neither IFN-γ nor IL-17. Similar findings were observed in T cells isolated from the retina during the early stages of EAU. NR4A2 expression by IL-17-secreting T cells in EAE was detected first in the target organ then later in the blood (Fig. 1D&E), which was concordant with the kinetics of NR4A2 expression in total lymphocytes (Fig. 1A).

NR4A2 Expression is not Detected in STZ-induced Diabetes or following OVA Immunization

We next measured NR4A2 expression in T cells from streptozotocin (STZ)-induced autoimmune diabetes [35], in which autoimmune Th1 cells but not Th17 cells are thought to play a pathogenic role [31]. Repeated administration of low-dose streptozotocin (STZ) induced anti-pancreatic autoimmunity accompanied with clinical diabetes by day 10 (Fig. S1C). Consistent with a previous report [35], splenocytes as well as pancreata-infiltrating T cells produced raised levels of IFN-γ, but not IL-17, after *in vitro* stimulation (Fig. S1D). Unlike CNS-infiltrating T cells in EAE, NR4A2 upregulation was not detected amongst pancreata-infiltrating T cells (Fig. 1F). We also examined blood T cells from these mice and detected no NR4A2 upregulation at any time (Fig. S1E). Furthermore, we examined if NR4A2 upregulation might be induced by active immunization with any antigen in CFA. However, immunization with OVA in CFA, using the same protocol for inducing EAE with MOG peptide, did not lead to NR4A2 upregulation.

NR4A2 Expression is Required for IL-17 Production by $ROR\gamma t^+$ T cells

As NR4A2 expression appeared to be associated with IL-17-secreting pathogenic T cells, we speculated that NR4A2 might function in the process of Th17 cell differentiation. Using NR4A2-specific siRNA, we investigated *in vitro* if $CD4^+$ T cells differentiate normally into Th1 or Th17 cells in the absence of NR4A2 regulation. Activation of T cells leads to a rapid and transient upregulation of NR4A2 that could be prevented by transfection with NR4A2 siRNA (Fig. S2A). When NR4A2 expression was silenced in this manner, naïve $CD4^+$ T cells were able to differentiate into IFN-γ-producing cells (Fig. 2A&C), excluding a requirement for NR4A2 in Th1 cell development. However, blocking NR4A2 upregulation with siRNA greatly reduced Th17 differentiation driven by any concentrations of TGF-β, as assessed by an absence of IL-17 production (Fig. 2B&C), instead there was an increase in IFN-γ-secreting T cells. We also noted that NR4A2 knockdown did not significantly reduce the proliferation of $CD4^+$ T cells under any polarizing conditions tested (Fig. S2B), indicating that NR4A2-specific siRNA is unlikely to prevent IL-17 production by affecting cell survival. Intriguingly, despite the lack of IL-17 production in the absence of NR4A2, T cells did upregulate RORγt, the hallmark transcription factor of Th17 cells, to levels comparable to fully functional Th17 cells (Fig. 2D).

Lack of IL-17 in the Absence of NR4A2 does not Result from the Action of Foxp3

A previous study has described a failure of RORγt-expressing Th17 cells to secrete IL-17 resulting from a direct inhibitory interaction between RORγt and the transcription factor Foxp3 [36]. To examine if a similar mechanism, involving Foxp3, is applicable to interpreting our results, we measured the level of Foxp3 expression during NR4A2 knockdown. NR4A2 siRNA did not enhance but reduced Foxp3 expression in both Th17 (TGF-β+IL-6) and regulatory T cell (TGF-β alone) differentiating conditions (Fig. S3A). This finding is consistent with a recent report on a role of NR4A2 for inducing Foxp3 in regulatory T cells [37]. Furthermore, we tested if NR4A2 ablation by siRNA treatment was still effective in preventing IL-17 production when Foxp3 expression was blocked. To do this, we used Foxp3-specific siRNA to prevent Foxp3 expression in T cells that also received either control or NR4A2-specific siRNA. Foxp3 knockdown did not restore IL-17 production in the absence of NR4A2 (Fig. S3B).

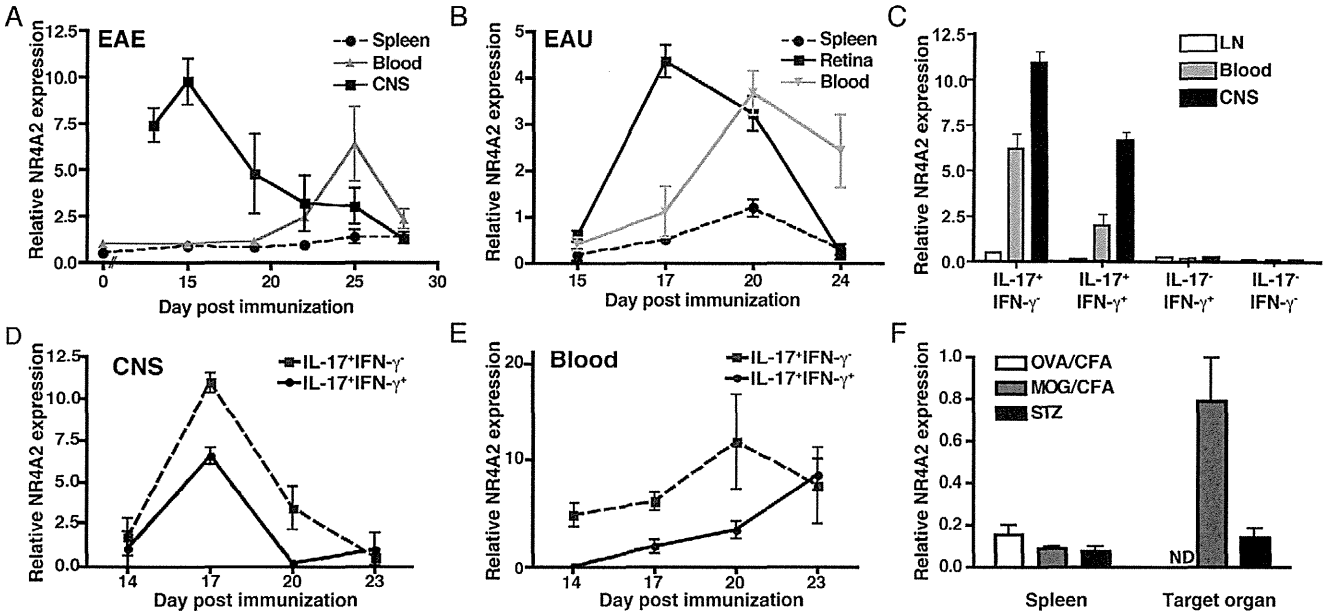

Figure 1. Autoimmune induction of NR4A2 in CD4$^+$ T cells is associated with IL-17-secreting T cells. EAE or EAU was induced in C57BL/6 mice by immunization with MOG_{35-55} or $IRBP_{1-20}$ peptide in CFA, respectively. CD4$^+$ T cells were purified from spleen, blood, or target organ (CNS or retina) on the indicated days and RNA was isolated. **A** and **B:** NR4A2 expression was quantified by real time PCR relative to GAPDH for T cells from EAE (A) or EAU (B). Timepoints correspond to a minimum of 5 animals and data are representative of 3 independent experiments. CD4$^+$ T cells from mice with EAE were restimulated with PMA/ionomycin for 3 hours and 4 populations of cytokine secreting cells (IL-17+IFN-γ-, IL-17+IFN-γ+, IL-17-IFN-γ+, and IL-17-IFN-γ-) were sorted by flow cytometry using IFN-γ and IL-17 cytokine secretion assay kits. **C:** NR4A2 expression by populations of cytokine-secreting CD4$^+$ T cells was quantified by real time PCR at day 15 post-EAE induction for lymph nodes (LN) and CNS-infiltrating cells (CNS), and day 25 for blood T cells. **D** and **E:** NR4A2 expression by IL-17$^+$IFN-γ$^-$ or IL-17$^+$IFN-γ$^+$ CNS-infiltrating T cells (**D**) or blood T cells (**E**) was measured by real time PCR at a range of timepoints. Data are representative of 2 independent experiments. **F:** Th1-mediated diabetes was induced in C57BL/6 mice by 5 daily low dose STZ treatments. Other groups of C57BL/6 mice were immunized with peptides in CFA plus PTX either $OVA_{323-339}$ (OVA/CFA) or MOG_{35-55} (MOG/CFA). On day 22, NR4A2 expression was assessed by real time PCR amongst CD4$^+$ T cells from spleen and leukocytes isolated from the relevant target organ (ND, OVA/CFA; CNS, EAE; pancreas, STZ). Timepoints correspond to a minimum of 5 animals and data are representative of 2 independent experiments.
doi:10.1371/journal.pone.0056595.g001

Thus, NR4A2 appears to be required for IL-17 production by Th17 cells, and the underlying mechanism is independent of RORγt and Foxp3.

NR4A2 Controls the IL-21-initiated Phase of Th17 Differentiation

RORγt expression is required for generation of fully functional Th17 cells. However, when upregulation of NR4A2 is prevented, Th17-polarized RORγt$^+$ T cells do not acquire the ability to produce IL-17 (Fig. 2). A possible scenario is that RORγt regulation is an early event in Th17 differentiation [38], whereas later induction of NR4A2 is critical for inducing signals that promote IL-17 production. IL-21-deficient or IL-21R-deficient T cells resemble NR4A2-deficient T cells in that they express RORγt but do not produce IL-17 under Th17 polarizing condition [4,39]. Thus, we suspected that NR4A2 expression might control IL-17 production via autocrine IL-21 signalling. IL-21 is produced during early Th17 cell differentiation and then acts in an autocrine manner to induce IL-23R upregulation by Th17 cells [38,40]; the subsequent action of IL-23 produced by myeloid cells then enhances and stabilizes the Th17 cell phenotype via IL-23R. To clarify the kinetics of these key molecules, we evaluated the expression of IL-21, IL-23R, and IL-17 transcripts by RORγt$^+$ T cells during *in vitro* Th17 cell differentiation. IL-21 begins to be produced before IL-23R is upregulated, which itself precedes IL-17 expression (Fig. 3A). Interestingly, NR4A2 siRNA transfection strongly inhibited the sequential regulation of IL-21, IL-23R, and IL-17 RNA transcripts (Fig. 3A). We also confirmed the reduction of IL-21 by NR4A2 siRNA treatment at the protein level (Fig. 3B). These data indicate that NR4A2 may be required for IL-21 production and thus in turn control Th17 differentiation. Furthermore, the lack of NR4A2 also blocked c-maf upregulation (Fig. 3C), a transcription factor reported to control IL-21 expression in Th17 development [41]. Finally, Th17 differentiation yields normal IL-22 production in the absence of NR4A2 (Fig. 3D) and the generation of IL-22 has been shown to be related to pathways downstream of RORγt, but independent of c-maf, IL-21, and IL-23 signalling [42]. To test the hypothesis that NR4A2 is required for full Th17 differentiation due to its role in the c-maf/IL-21/IL-23R pathway, we reintroduced this pathway by adding exogenous IL-21 to cultures. Critically, the presence of exogenous IL-21 restored IL-17 secretion by T cells stimulated under Th17 polarizing conditions despite the lack of NR4A2 (Fig. 4A). Additionally, NR4A2-knocked down Th17 cells cultured with IL-21 also expressed equivalent levels of IL-23R to the control Th17 cells (Fig. 4B).

NR4A2 Controls the Severity of EAE

Next we tested if NR4A2 also controlled pathogenic Th17 responses in EAE. Administration of NR4A2-specific siRNA on the day of EAE induction was effective at preventing NR4A2 expression by CNS-infiltrating T cells (Fig. S4A). Such systemic blockade of NR4A2 suppressed the onset of clinical EAE (Fig. 5A), accompanied by a reduced ability of CNS-infiltrating CD4$^+$ T

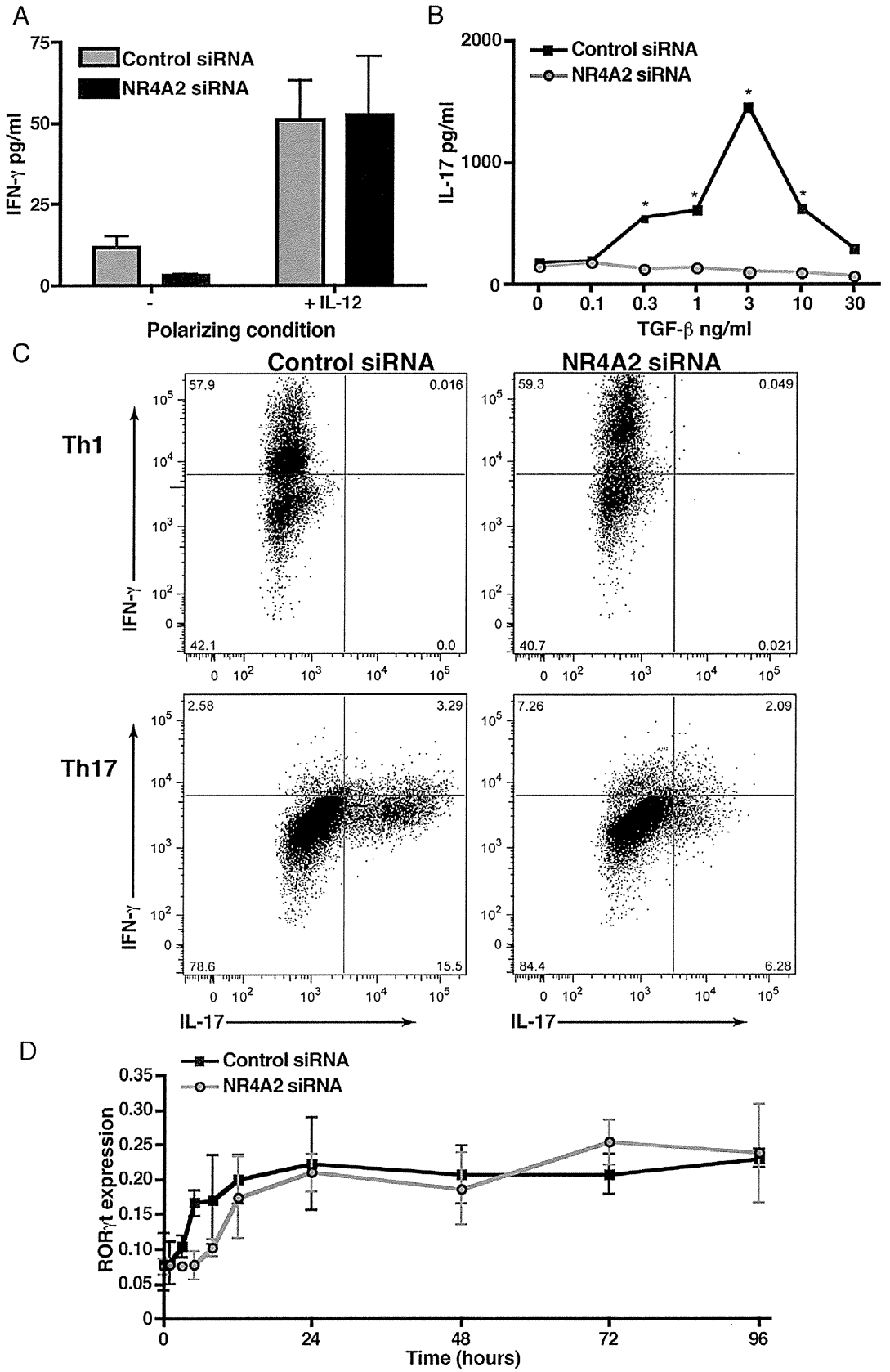

Figure 2. NR4A2 knockdown prevents IL-17 secretion but not RORγt upregulation. Naïve CD4$^+$ T cells were transfected by electroporation with NR4A2-specific siRNA or scrambled control siRNA. Cells were then activated with 5 μg/ml plate-bound CD3-specific mAb and 0.5 μg/ml soluble CD28-specific mAb. **A:** IFN-γ production by cells activated in the presence or absence of 10 ng/ml IL-12 after 96 hours of culture. **B:** IL-17 production

by cells activated in the presence of 20 ng/ml IL-6, 20 ng/ml IL-23, and TGF-β at a range of concentrations after 96 hours of culture. Significant differences between control and NR4A2 siRNA-treatments were tested with a student's t-test, *p<0.05. **C:** IL-17 and IFN-γ intracellular cytokine staining for transfected T cells (control siRNA, left plots; NR4A2 siRNA, right plots) cultured for 96 hours in the presence of 10 ng/ml IL-12 (Th1 conditions, top row plots) or 20 ng/ml IL-6, 20 ng/ml IL-23, and 3 ng/ml TGF-β (Th17 conditions, bottom row plots). **D:** RORγt RNA expression as measured by real time PCR by activated T cells cultured under Th17 polarizing conditions at a range of timepoints. Data are representative of 5 independent experiments.
doi:10.1371/journal.pone.0056595.g002

cells to secrete IL-17 but not IFN-γ (Fig. 5B) when restimulated with the immunizing peptide. NR4A2 siRNA treatment also led to a lower proportion of T cells in the target organ that produced IL-17 upon non-specific restimulation during early timepoints (summarized in Fig. 5C; representative data, Fig. S4B). However, we observed that the effect of NR4A2 siRNA is not persistent, and the mice showed signs of late onset EAE after day 21 (Fig. 5A) accompanied by an increase in the proportion of IL-17$^+$ T cells in the CNS (Fig. 5C). Since collagen-stabilized siRNA maintains its suppressive activity *in vivo* for approximately three weeks [43], the

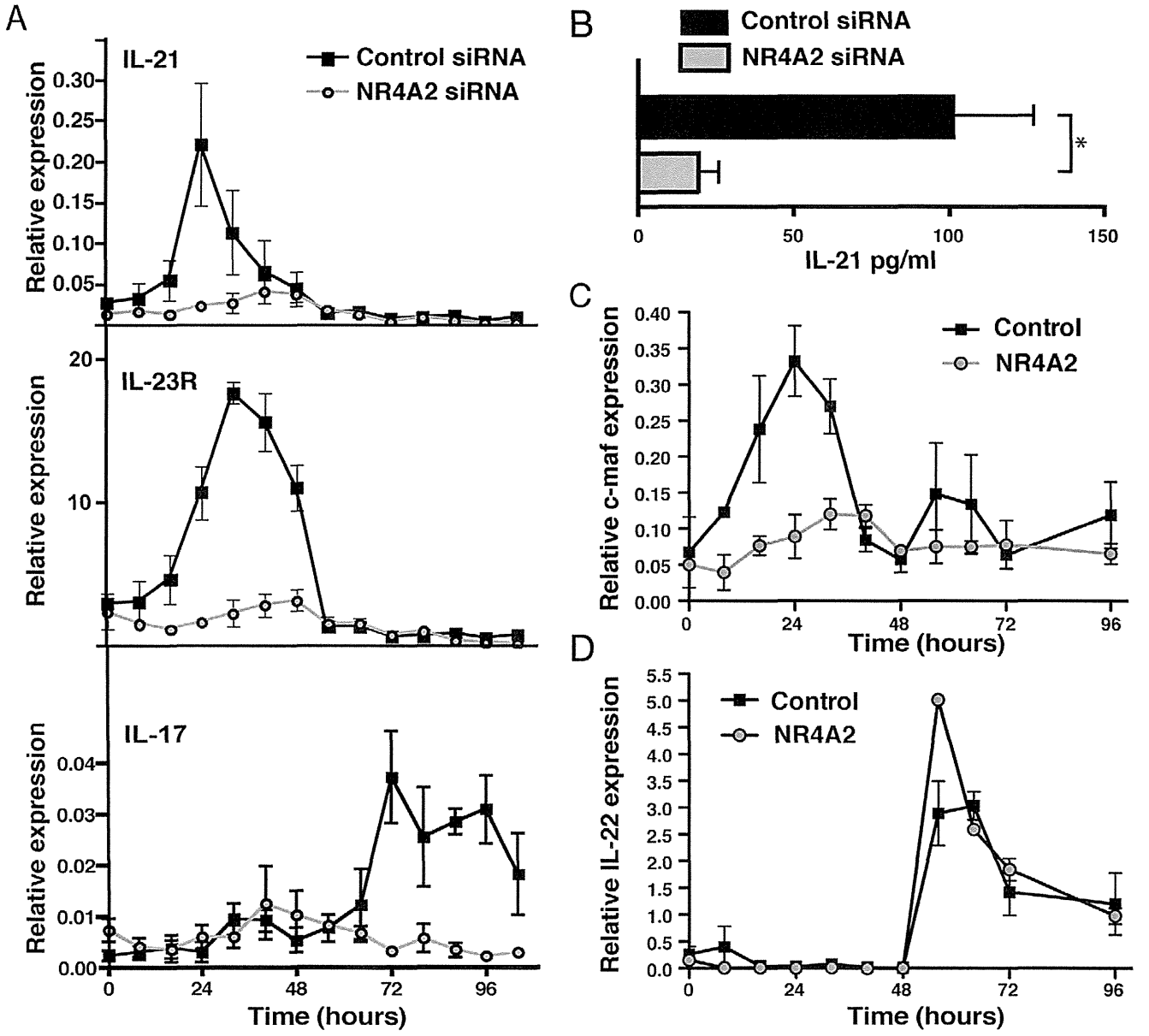

Figure 3. Absence of NR4A2 is associated with a lack of IL-21 production by Th17 cells. Naïve CD4$^+$ T cells were transfected by electroporation with NR4A2-specific siRNA or scrambled control siRNA and were activated with 5 μg/ml plate-bound CD3-specific mAb and 0.5 μg/ml soluble CD28-specific mAb in the presence of 20 ng/ml IL-6, 20 ng/ml IL-23, and 3 ng/ml TGF-β. **A:** RNA levels of IL-21, IL-23R, and IL-17 were quantified by real time PCR at the indicated timepoints following activation. Data are representative of 3 independent experiments. **B:** IL-21 supernatant concentration was measured by ELISA at 96 hours. Data are representative of 3 independent experiments. *p<0.05. **C:** RNA expression of c-maf quantified by real time PCR. **D:** RNA expression of IL-22 quantified by real time PCR. Data are representative of 2 independent experiments.
doi:10.1371/journal.pone.0056595.g003